SCIENCE CHINA Materials REVIEWS

mater.scichina.com link.springer.com

Sci China Mater 2023, 66(7): 2545–2572

Recent development in metal halide perovskites synthesis to improve their charge-carrier mobility and photocatalytic efficiency

Marija Knezevic[1], Thi-Hieu Hoang[1], Nusrat Rashid[2], Mojtaba Abdi-Jalebi[2], Christophe Colbeau-Justin[1] and Mohamed Nawfal Ghazzal[1*]

ABSTRACT Over the past decade, all-inorganic metal halide perovskites (MHPs, $CsPbX_3$: X = Cl, Br, I) have been widely investigated as promising materials for optoelectronic devices such as solar cells and light-emitting diodes. MHPs are defect-tolerant, which allows tuning of their bandgap without altering their photophysical properties. From a fundamental point of view, MHPs are excellent candidates for photocatalytic reactions due to their light-harvesting capability, high photogenerated charge-carrier mobility, long diffusion lengths, and tunable bandgap energy. In this review, we provide an overview of various MHP engineering strategies (e.g., surface, morphological, and structural modifications, heterojunction coupling, and encapsulation) which are directly linked to the charge-carrier mobility and lifetimes, and then to the photocatalytic efficiency. Specifically, we outline different synthetic approaches resulting in surface and morphological modifications, anion/cation substitution, metallic doping, coupling, and encapsulation that tremendously influence MHPs' stability, optical properties, and charge-carrier dynamics at variable time scales (from fs to µs). We also provide an in-depth evaluation of the MHPs for variable photoredox reactions, discussing how the optical and electronic properties help to improve their stability and efficiency.

Keywords: all-inorganic halide perovskite, charge-carrier dynamics, stability, photocatalysis

INTRODUCTION

In the last decade, all-inorganic metal halide perovskites (MHPs) $CsPbX_3$ (X = Br, Cl, I) have received a close review of the photochemical and photoelectrochemical communities, although their stoichiometry [1], crystallinity [2,3], and photoconductivity [4] have been known for more than a century. The successful story of perovskites started in 1840, when the term perovskite was firstly used by German mineralogist Gustav Rose to describe the newly discovered ABX_3 compound during his exploratory expedition in Russia, i.e., $CaTiO_3$, in honor to Lev Alekseyevich Von Perovski, a Russian mineralogist [5]. Since then, this naming was widely accepted as a common designation for all ABX_3 materials [6]. Later in 1893, compounds based on cesium, lead, and halides from aqueous solutions, $CsPbX_3$ (X = Br, Cl, I), were reported, as well as non-perovskite structures such as Cs_4PbX_6 and $CsPb_2X_5$ (X = Br, Cl) [1]. The first detail of crystalline MHP structure was revealed for the high-temperature $CsPbI_3$ perovskite phase in 1958 [2]. Two phases were described, the black cubic and yellow orthorhombic. The latter is a non-perovskite phase but thermodynamically favored and stable under ambient conditions. The cubic crystals of $CsPbCl_3$ and $CsPbBr_3$ were found to be formed at a temperature above 320 and 400 K, respectively [3]. The phase transition studies of MHPs showed the transformation from orthorhombic through tetragonal to cubic phase with the temperature increase, and even monoclinic $CsPbCl_3$ at a temperature lower than 310 K (Table 1) [7].

It is worth mentioning that with the expansion of both hybrid and all-inorganic perovskites, the term "perovskite" has been employed for all compounds containing Cs, Pb, and Br atoms, regardless of their ratio [8–11]. Breternitz and Schorr [12] emphasized the importance of defining perovskite as a crystalline structure ABX_3 (or A:B:X = 1:1:3), with B cation having either octahedral or distorted octahedra coordination, organized in an all-corner three-dimensional (3D) sharing network. Since 0D, 1D, and 2D, e.g., Cs_4PbX_6 and $CsPb_2X_5$, do not share such properties, they are considered as non-perovskite structures. More recently, Akkerman and Manna [13] explained different metal halide lattice distortions, distinguishing cubic, anti, distorted, vacant, ordered, and vacancy-ordered perovskites. Due to the size difference of the A, B cations, and X anion, halide perovskites usually suffer from certain distortions and do not crystalize in perfect cubic phase (aristotype), but rather experience lower symmetry (hettotype). What has to be taken into account when describing a crystallite as halide perovskite is certainly its stability with Goldschmidt tolerance factor (t, $0.80 \leq t \leq 1.00$) [6,14,15], and octahedral factor ($\mu > 0.41$) [14,15].

In the following fifty years, the optical and electronic properties of MHPs have been discussed, including their application for the X-ray and γ-ray radiation detection [20–25]. Despite the quantum confinement effect of $CsPbX_3$-like quantum dots (QDs, X = Br, Cl) in CsX single-crystal host (X = Cl, Br), being known since 1997 [23], it was only after the breakthrough of $CsPbX_3$ nanocrystals (NCs) colloidal synthesis in 2015 that the astonishing development of MHP NCs synthetic methods has been recorded [19]. Further photophysical studies disclosing high photoluminescence quantum yield (PLQY), charge-carrier mobility, and diffusion lengths, i.e., the micrometer range, have followed [26–28]. By the time the first research of MHP-based

---

[1] Université Paris-Saclay, Institut de Chimie Physique, UMR 8000 CNRS, 91405, Orsay, France

[2] Institute for Materials Discovery, University College London, Malet Place, London, WC1E 7JE, UK

[*] Corresponding author (email: mohamed-nawfal.ghazzal@universite-paris-saclay.fr)

Table 1 Structural properties of all-inorganic perovskites $CsPbX_3$

	Lattice parameters (Å)			Space group	Crystal symmetry	Phase transition temperature (K)	Ref.
	a	*b*	*c*				
$CsPbCl_3$	5.607	5.575	5.572	*Pmmm*	orthorhombic	$315 > T > 310$	[3,7,16]
	5.590	5.590	5.630	*P4/mbm*	tetragonal	$320 > T > 315$	
		5.605		*Pm-3m*	cubic	320	
$CsPbBr_3$	8.207	8.255	11.759	*Pbnm*	orthorhombic	Ambient	[4,17]
	5.827	5.827	5.891	*P4/mbm*	tetragonal	266–397	
		5.874		*Pm-3m*	cubic	410–500	
$CsPbI_3$	10.028	4.853	18.164	*Pnma*	orthorhombic (δ)	Ambient	[18,19]
	6.095	6.259	6.250	*Pbnm*	orthorhombic (γ)	325	
	6.241	6.241	6.299	*P4/mbm*	tetragonal (β)	510	
		6.297		*Pm-3m*	Cubic (α)	645	

solar cell was proposed [29], hybrid organic-inorganic perovskite solar cells had already been extensively investigated [30–33]. The iodine-based MHPs strike immense attention due to their small bandgap of 1.73 eV [34]. However, their rapid phase transformation and relatively limited stability prevent the extension of their field of application. The ongoing studies are focused on their stability improvement; e.g., it is shown that heating up the yellow non-perovskite phase (δ-perovskite) results in the orthorhombic perovskite phase upon cooling (γ-perovskites), allowing longer stability under ambient conditions [35]. Up to date, perovskite-silicon tandem solar cells registered the energy conversion efficiency record, reaching up to 31.3%, while single-junction perovskite solar cells reached the efficiency of 25.7% [36], being in close competition with the conventional thin-film and silicon solar cells. The MHPs have been used in a wide range of applications, being identified as promising materials for optoelectronics [27,37,38], and very recently photocatalysis, which will be discussed thoroughly in this review. Besides being optically active in a large range of the solar spectrum, to be considered as an efficient photocatalyst, MHPs should be able to convert quantum energy to highly mobile and long-lived charge carriers and overcome instability to moisture, non-polar media, and illumination-induced phase segregation. In general, the stability and photoelectronic properties of MHPs, which determine their photocatalytic efficiency, are elaborated through MHP coating with stable materials, and selective control of the synthetic procedure of MHPs. In this review, we will first expose diverse synthetic procedures reported up to now, which offer great flexibility and versatility in morphology control, electronic bandgap engineering, and enhancement of charge carriers' lifetime. Then, an overview of the photoelectronic properties and their evolution through a selective substitution of the anion (or cation) atom in terms of light-harvesting properties will be discussed [19,39–55]. The last part is dedicated to the recent advancements and achievements of MHPs as a photoactive photocatalyst.

SYNTHETIC METHODS FOR CSPBX$_3$ NCs

The time- and energy-consuming protocols are the main challenges facing industrial scale-up MHP synthesis, while keeping excellent dispersion, size distribution, structural, optical, and photophysical properties of NCs. NC colloidal hot injection method [19] has led to the development of different synthetic procedures such as microwave (MW)-assisted synthesis [56–60], ultrasonication (US) [48,61–63], solvothermal (SV) method [64–69], ligand-assisted reprecipitation (LARP) [70,71], post-synthetic anion exchange [39,50], cation exchange [52], and conversion of Cs_4PbX_6 [72–75]. Here, we will discuss the versatility of different synthetic methods that yield nanocubes (NCus), nanowires (NWs), nanorods (NRs), nanoplatelets (NPLs), and nanosheets (NSs), as well as their advantages and emerging green perovskite synthesis [76–78].

Direct synthesis of MHPs

Hot-injection method

The extensively used hot-injection method consists of a quick injection of cesium-oleate (Cs-oleate) in the solution of PbX_2 (X = Br, I, Cl) in octadecene (ODE), containing oleylamine (OAm), and oleic acid (OA) as capping agents, under inert gas or vacuum, followed by immediate quenching in the ice water bath:

$$2Cs(RCOO) + 3PbX_2 \rightarrow 2CsPbX_3 + Pb(RCOO)_2. \tag{1}$$

The reaction is performed in the temperature range of 140–200°C allowing variation of the particle size in the range of 4–15 nm (Fig. 1a) [19]. The Cs-oleate is prepared separately by mixing cesium-carbonate (Cs_2CO_3) or cesium-acetate (CsOAc) with OA in ODE at 120°C:

$$Cs_2CO_3 + 2RCOOH \rightarrow 2Cs(RCOO) + CO_2 + H_2O. \tag{2}$$

The advantage of using Cs-acetate lies in its non-hygroscopic nature and the liquid state of Cs-oleate upon cooling [79]. However, Lu *et al.* [80] demonstrated that Cs_2CO_3 can be completely dissolved with the ratio of Cs:OA = 1:5, allowing complete solubility at room temperature, making $CsPbBr_3$ synthesis independent on Cs-oleate precursor origin (Fig. 1b, c). Cs-oleate in ODE is then heated and injected into the mixture of Pb-oleate and OAm-X (3) to trigger the formation of $CsPbX_3$ and oleylammonium oleate (4). The metathesis reaction completion is driven by an excess of PbX_2 relative to $CsPbX_3$ [81]:

$$PbX_2 + 2RCOOH + 2R'NH_2 \rightarrow Pb(OOCR)_2 + 2R'NH_3X \ (X = Br, I), \tag{3}$$

$$Cs(RCOO) + Pb(OOCR)_2 + 3R'NH_3X \rightarrow CsPbX_3 + 3R'NH_3OOCR \ (X = Br, I), \tag{4}$$

where, $R = CH_3(CH_2)_7HC{=}CH(CH_2)_7$, $R' = CH_3(CH_2)_7HC{=}CH(CH_2)_8$.

The MHPs' morphology can be controlled by adjusting the injection rate of Cs-oleate, during the synthesis of $CsPbI_3$ NCs, forming either NCus ($0.4\ mL\ s^{-1}$) or NRs ($0.4\ mL\ min^{-1}$) (Fig. 1d); on the contrary, the injection rate has no impact on

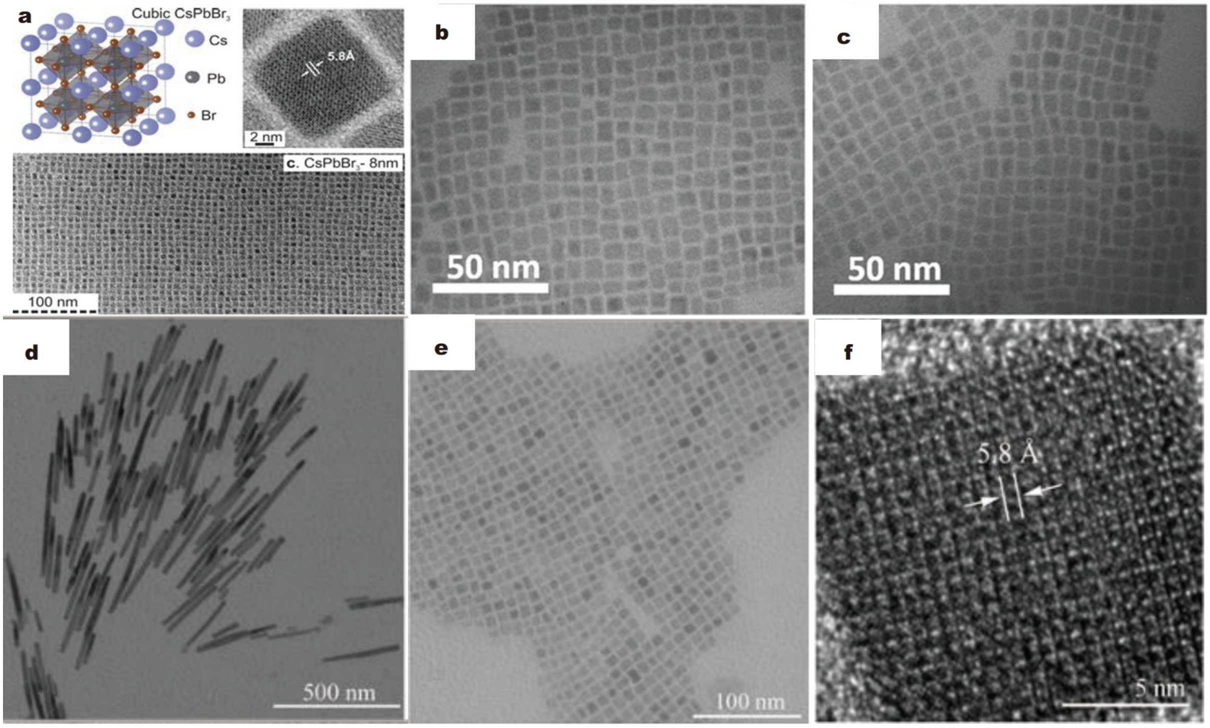

Figure 1 (a) High-resolution transmission electron microscopy (HRTEM) and TEM images of CsPbBr$_3$ and structural model of CsPbBr$_3$ (inset). Reprinted with permission from Ref. [19], Copyright 2015, American Chemical Society. (b) CsPbBr$_3$ prepared with Cs-oleate (OAc) and (c) Cs-oleate (CO$_3$) with Cs:OA ratio 1:5. Reprinted with permission from Ref. [80], Copyright 2018, American Chemical Society. (d) Effect of the injection rate of 0.4 mL min^{-1} on CsPbI$_3$ NRs and (e, f) CsPbBr$_3$ NCu synthesis. Reprinted with permission from Ref. [82], Copyright 2017, Elsevier B.V.

CsPbBr$_3$ morphology (Fig. 1e, f) [82].

Significant attention was dedicated to the influence of different capping agents, i.e., carboxylic acids and alkyl amines, on NC stability [83–85]. A variation of acid/amine ratio, chain length, and temperature dictates the control of the shape, size, and morphology of the MHPs, giving rise to NCus, NPLs and NSs (Fig. 2) [79,83,86]. The long-chain capping agents, i.e., OA/OAm mixture, and their density control enhance NCs' surface passivation, a feature crucial for improving PL in light-emitting diode (LED) manufacturing [87,88]. However, during the purification process, MHPs could suffer from ligand loss, due to the proton transfer between acid and base, lowering NC stability [88,89].

The aging of PbBr$_2$ and Cs-oleate reaction, along with variation of temperature and capping agents, yields CsPbBr$_3$ NWs and CsPb$_2$Br$_5$ NSs, making this method perfect for synthesizing NCs with different photophysical properties (Fig. 3a–f) [90,91].

Versatile synthetic approaches demonstrated that the Pb/Cs ratio determines the phase purity of CsPbBr$_3$ synthesis: the copious amount of Cs leads to the formation of UV-active Cs$_4$PbBr$_6$, while the poor quantity of Cs results in the inhomogeneous cubic CsPbBr$_3$ NCs (Fig. 3g–i) [72,74,82,92–94]. Jing *et al.* [92] verified the influence of each Cs, Pb and Br on the final product composition, by mixing variable amounts of cesium acetate, lead acetate, and tetraoctylammonium bromide (TOAB) in the amine-free environment. The authors found that the influence of bromide is weak compared with the Pb/Cs ratio, which determines the phase purity. In addition, the introduction of OAm results in strong coordination of Pb^{2+} cations, causing their reduced availability, indulging the formation of Cs$_4$PbBr$_6$ (Fig. 3j–l). Simultaneously, it was revealed that the bromide concentration dictates the mechanism of MHP synthesis through CsBr-seeded growth of CsPbBr$_3$ [95], indicating two possible paths of CsPbBr$_3$/Cs$_4$PbBr$_6$ evolution [96].

It should be pointed out that the aging of CsPbBr$_3$ seed-clusters at 230°C results in the formation of polyhedron-shaped NCs that transform into hexapods with the addition of OAm-HBr solution (Fig. 4a–i). Polyhedrons and hexapods exhibit lower PL intensity compared with NCus, which makes them ideal for photocatalytic reactions [97]. Simultaneously, Bera *et al.* [98] replaced PbX$_2$ with PbO and α-halo ketone, i.e., phenacyl bromide, and found a synergic effect between phenacyl bromide and OAm forming tertiary amine upon aging at 180–220°C, through successive nucleophilic substitution (SN2) reactions (Fig. 4j). Bulky tertiary amine has a key role in synthesizing multifaceted morphologies due to the stabilization of dodecahedron facets (Fig. 4k). The shaping control of these MHPs leads to self-organization and self-assembly that could be developed to synthesize periodic nanostructures (Fig. 4k, l). Such a multifaceted synthetic approach could be beneficial for photocatalysis due to higher surface availability.

The hot-injection method provides well-dispersed and uniformed NCs, with controllable morphology, and it allows the direct synthesis of mixed halide perovskites. Nevertheless, it is a time-consuming method offering a very low yield. In light of what was previously discussed about ligand chain length, one should notice that the purity of OAm used in different studies varies from 70% to more than 90% [19,83,86,95]. OAm can contain up to 43% of its trans isomer, shorter chain, and unsaturated amines as well as oxygen-incorporated impurities [99]. Hence, replacing OAm would be one of the interests of ongoing research that will lead to scaling up MHP production for reproducible synthetic methods [100,101].

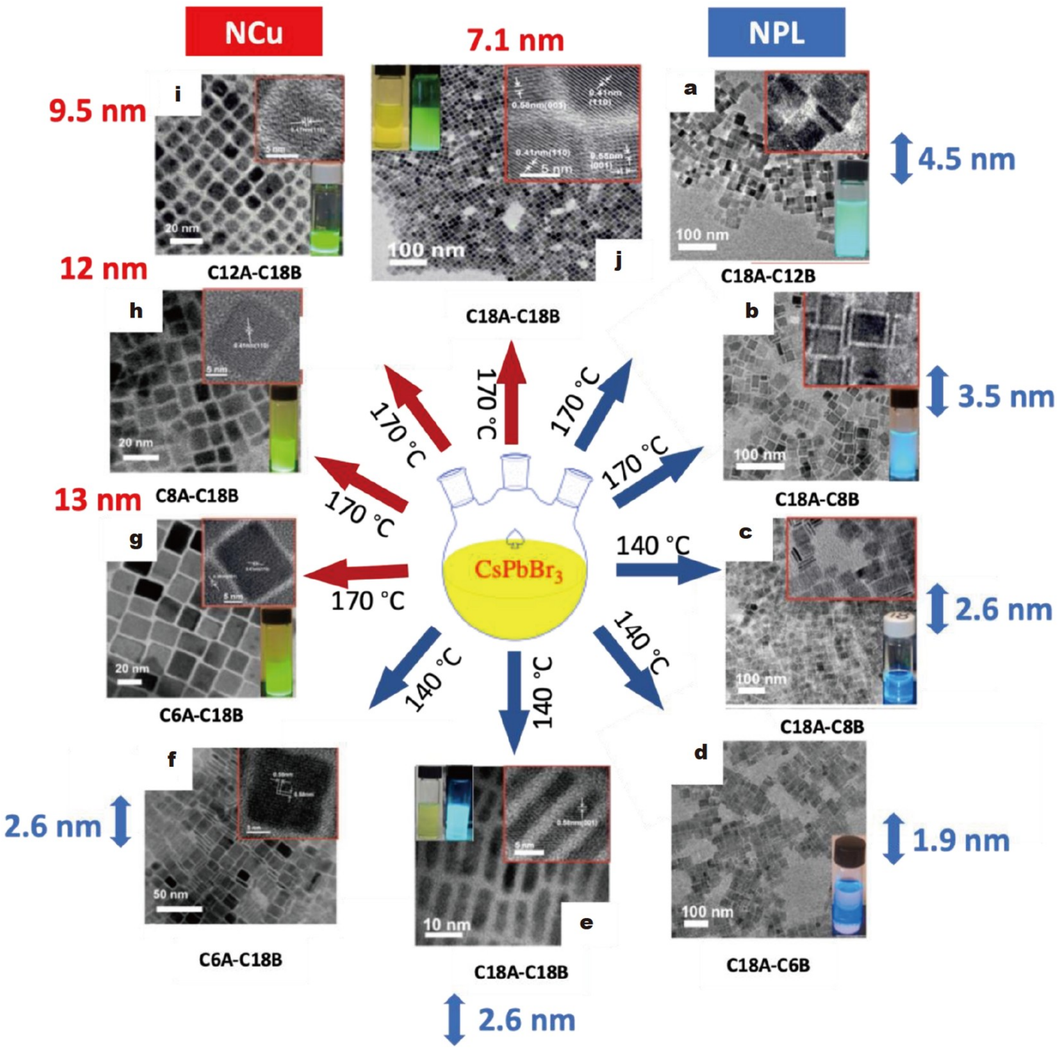

Figure 2 TEM and HRTEM images of $CsPbBr_3$ NPLs synthesized at 170°C using C18A-C12B and C18A-C8B, and at 140°C using C18A-C18B, C18A-C8B, C18A-C6B, and C6A-C18B. NCus synthesized using C18A-C18B, C12A-C18B, C8A-C18B, and C6A-C18B at 170°C, with the insets of $CsPbBr_3$ NPLs colloidal solutions in hexane under ultraviolet (UV) light. Reprinted with permission from Ref. [79], Copyright 2016, American Chemical Society.

Ligand-assisted reprecipitation method

The LARP is a room-temperature method involving the mixing and dissolving of CsX and PbX_2 (or their anionic mixtures) with OA and OAm in polar solvents, such as dimethyl formamide (DMF) and dimethyl sulfoxide (DMSO). Then DMF or DMSO solution is transferred dropwise in a non-polar solvent, such as toluene (Fig. 5a). Since the solubility of MHPs in toluene is lower than 10^{-7} g mL^{-1}, they recrystallize under stirring due to the supersaturation. This method produces NCus with a well-defined monoclinic crystalline phase, with sizes in the range of 9 to 13 nm. The LARP method provides surface self-passivation with halide anions leading to superior PLQY compared with the one obtained by the hot injection method [70]. Morphology can be engineered by varying reaction time and capping agent ratio [102].

An alternative approach aiming at pre-dissolving a mixture of Cs_2CO_3 and PbO in OA at 120°C is proposed to avoid the use of polar solvents that can damage NCs, i.e., DMF and DMSO. Upon cooling to room temperature, toluene and OA are added to the reaction mixture, followed by ammonium-bromide injection, yielding uniform MHPs with an average size of 7.8 nm. More importantly, this method allows OAm-free and gram-scale MHP production, yielding a uniform size of 8.4 nm (Fig. 5b, c) [71]. The LARP method offers rapid MHP preparation at ambient conditions with high PLQY, competitive to the time- and energy-consuming hot-injection synthesis.

Single-step microwave-assisted synthesis

The MW method offers efficient, quick, and controllable preparation of $CsPbBr_{3-y}X_3$ NCus, nanoplates, and NRs in only four to five-minute time due to its homogenous, selective, and high-rate heating [103,104]. The reaction time under 800 W should not exceed 4–5 min at the risk of losing the uniformity of the NCs [60]. To the best of our knowledge, only a few research groups have explored this procedure and its advantages [56–60]. Under MW, a quartz tube containing a mixture of CsOAc, PbX_2, trioctylphosphine oxide (TOPO), OA, OAm, and ODE is heated up to 160°C under air, yielding orthorhombic NCus of ~10.8 nm (Fig. 6a). By decreasing the temperature to 80°C, nanoplates (NPs) could be formed, while the pre-dissolving of precursors leads to NR morphology. The morphology of $CsPbI_3$ can be tuned by varying Cs/Pb ratio (NRs), by replacing OA with

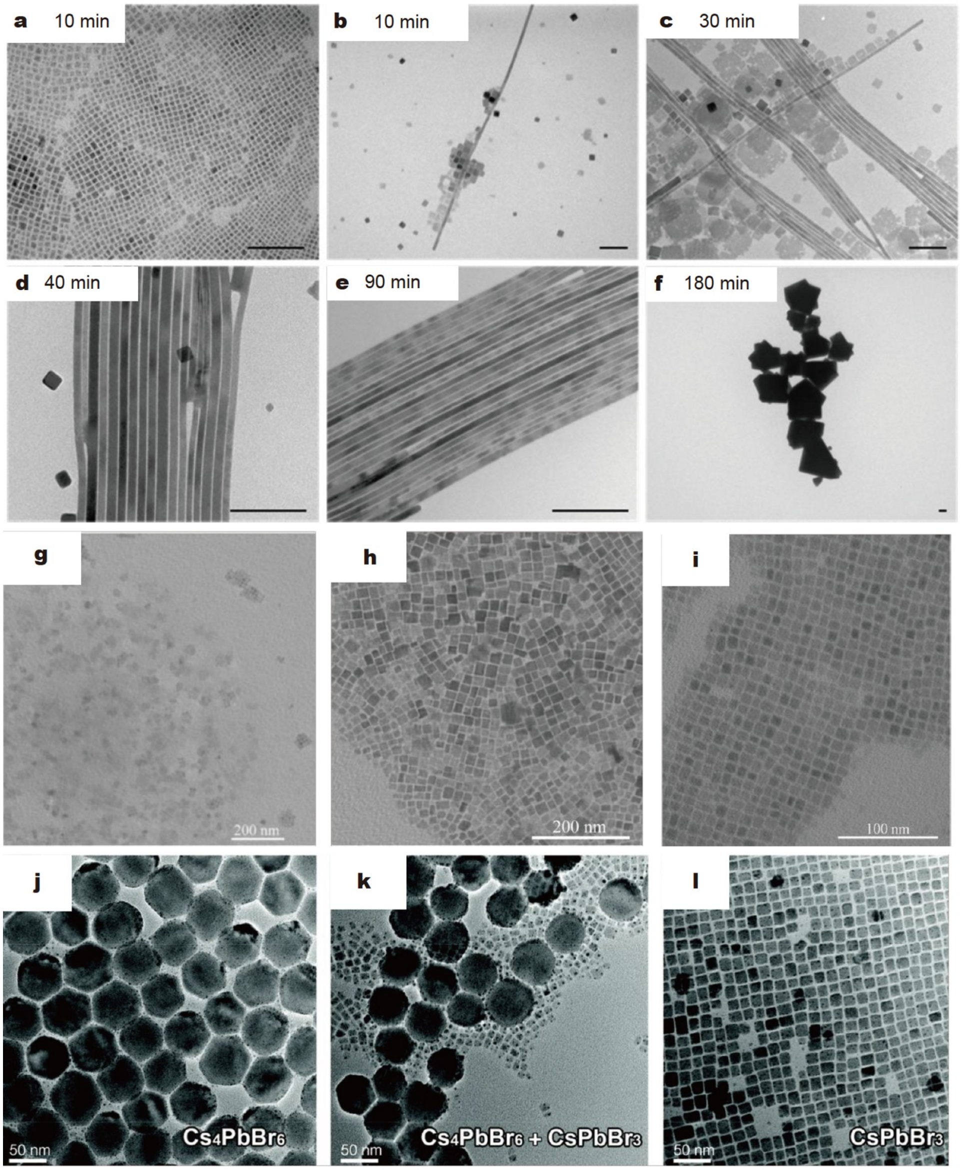

Figure 3 (a–f) TEM images of $CsPbBr_3$ NWs obtained at different reaction times. Scale bar corresponds to 100 nm. Reprinted with permission from Ref. [90], Copyright 2015, American Chemical Society. (g) $CsPbBr_3/Cs_4PbBr_6$ mixture due to excess of Cs-oleate, (h) non homogenous $CsPbBr_3$ due to insufficient Cs-oleate and (i) homogeneous $CsPbBr_3$, respectively. Reprinted with permission from Ref. [82], Copyright 2017, Elsevier B.V. (j–l) $CsPbBr_3$ morphologies when the amount of Cs/Pb/Br was fixed at (a) 4–1–6, (b) 4–4–6, and (c) 4–6–6 mmol. Reprinted with permission from Ref. [92], Copyright 2019, Royal Society of Chemistry.

octylamine (NWs), or by doubling ODE, OA, and OAm amounts (NPLs) [56]. Raising the temperature above 160°C leads to non-uniform size distribution and agglomeration due to the poor chelating effect of OAm/OA. The MW method offers control of the heating rate, demonstrating increasing particle size from 10.8 to 15.1 nm when the heating rate is decreased from 28 to 12°C min^{-1}. Slowing down the heating rate to 8°C min^{-1} leads to larger-sized NPs of 150 nm.

Slowing down the reaction rate while the reactants are separated on two different endings of the reactor, and a mixture of OAm, OA, and ODE is slowly poured into it, revealed the nucleation mechanism, confirming the formation of corner-sharing PbX_6 octahedra, being later stabilized by Cs^+ cations, so-called Lamer crystal growth (Fig. 6b). After 25 min, cubic well-crystalized $CsPbBr_3$ NCs are formed, with an edge length of 10–24 nm [57]. MW-assisted synthesis is a versatile method that offers the preparation of NCs with different morphologies and anion stoichiometry. It is an open-air and rapid method that produces uniform MHP with either monoclinic, orthorhombic, or cubic crystal lattice, owing to its highly controllable and rapid heating.

Ultrasonication synthesis method

The US method is a simple room-temperature method that includes direct mixing of precursors (Cs_2CO_3, PbX_2, OAm, OA, and ODE/mineral oil) without any pretreatment and pre-dissolving, followed by direct tip sonication at the energy of 30 W for 10 min (Fig. 7a) [48]. The US method is adequately adapted

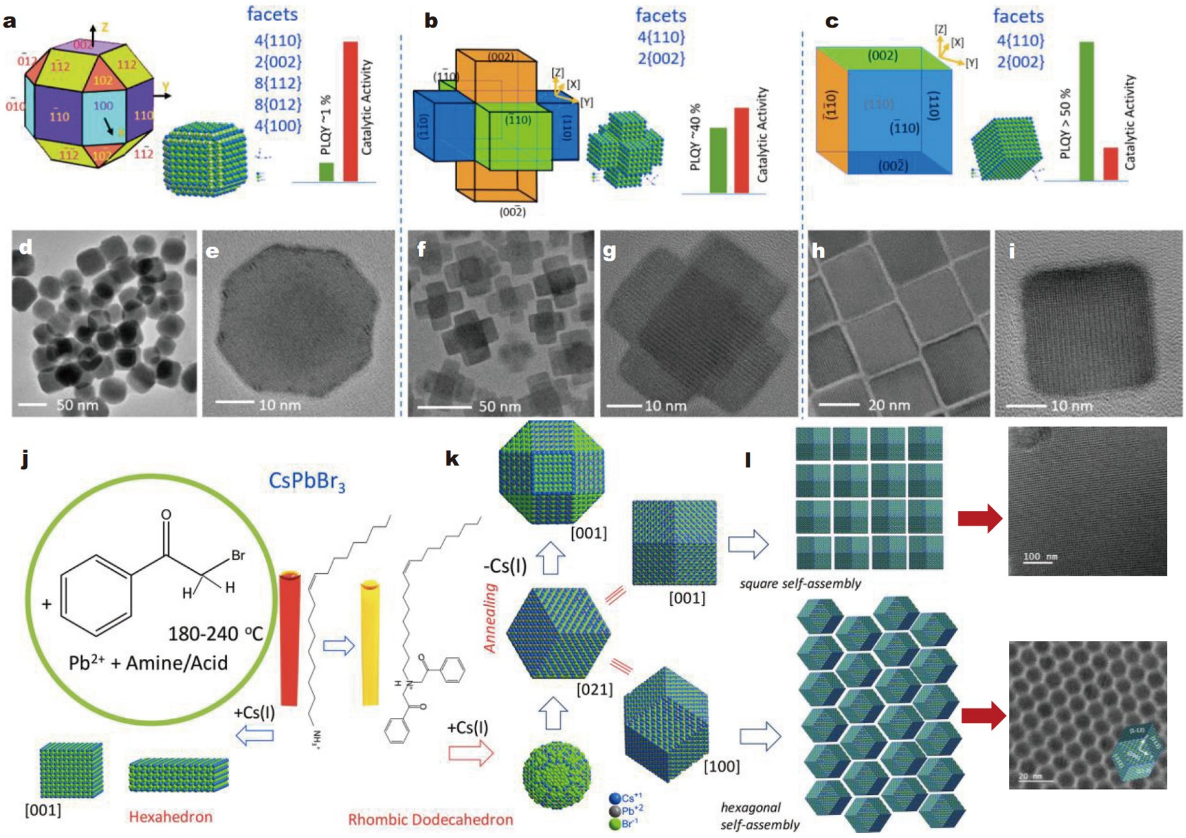

Figure 4 Schematic representations of (a) polyhedron, (b) hexapod, (c) cube-shaped MHPs, with their corresponding TEM images (d–i); (j) schematic representation of the synthesis of multifaceted NCs using PbO and phenacyl bromide, and the synergic effect of phenacyl bromide and OAm forming tertiary amine upon aging at 180–220°C upon immediate (red) and delayed (yellow) Cs injection; (k) nucleation of quasi-spherical dots, and formation of 12 faceted rhombic dodecahedron and 26 faceted rhombicuboctahedron; (l) self-assembly patterns of dodecahedrons in square and hexagonal close packing. Reprinted with permission from Refs [97,98], Copyright 2020, American Chemical Society.

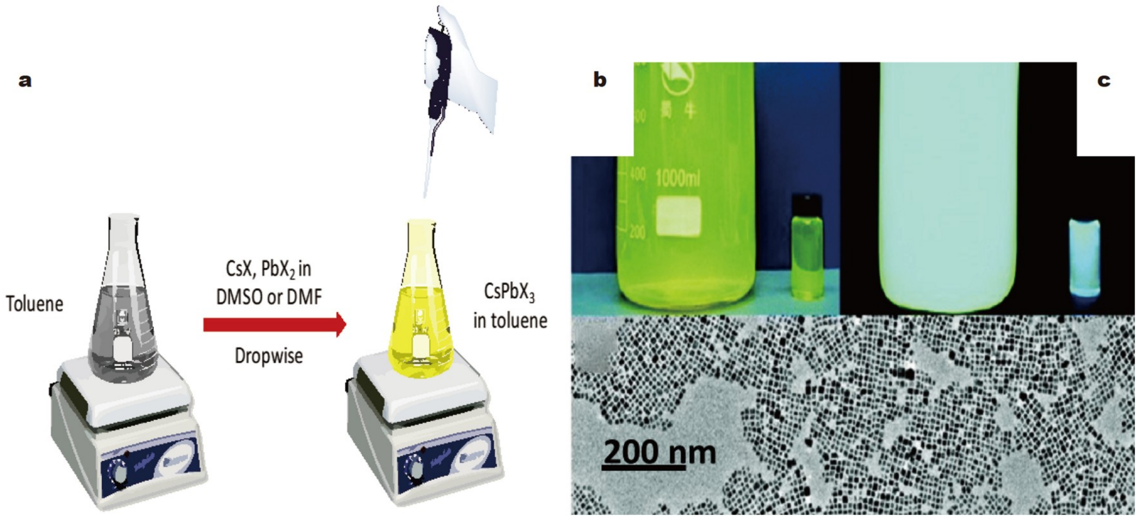

Figure 5 (a) Schematic representation of the LARP method; colloidal solution of gram-scale synthesis of CsPbBr$_3$ (b) before and (c) after illumination under UV light and the corresponding TEM images (scale bar: 200 nm). Reprinted with permission from Ref. [71], Copyright 2016, The Royal Society of Chemistry.

for the synthesis of mixed CsPbBr$_{3-y}$X$_y$ perovskites (Fig. 7b). The average size of CsPbBr$_{3-y}$X$_y$ NCus obtained through the seeded mechanism is in the range of 8–20 nm. Variation of the Cs/Pb ratio allows tuning of the NPLs' thickness. This method provides high PLQY, comparable to those obtained by the hot-injection method, at ambient temperature and open air, and it could be potentially scalable when the amount of each precursor is increased by tenfold (Fig. 7c) [48]. Increasing the amount of precursors for the factor of 10 and extending the reaction time to 30 min yields the supercrystals of a few hundred nm size

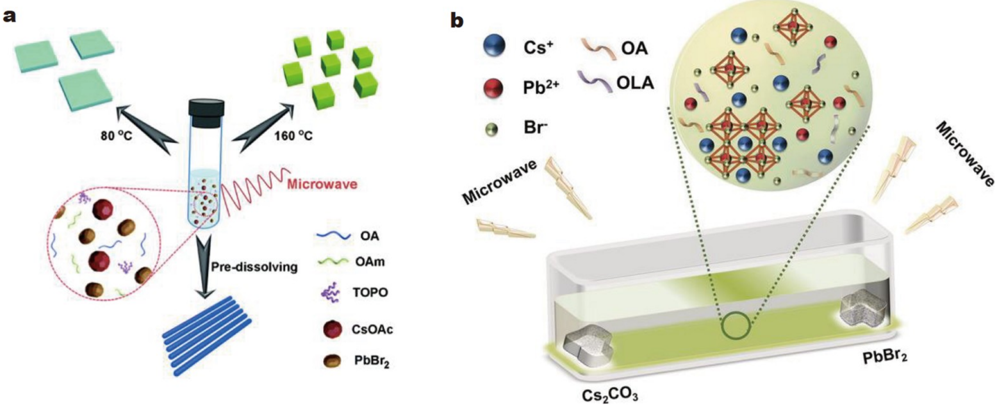

Figure 6 (a) Schematic representation of slowed down MW-assisted synthesis. Reprinted with permission from Ref. [56], Copyright 2018, Wiley-VCH Verlag GmbH &Co. KGaA, Weinheim. (b) Schematic representation of one-pot MW-assisted synthesis. Reprinted with permission from Ref. [57], Copyright 2017, The Royal Society of Chemistry.

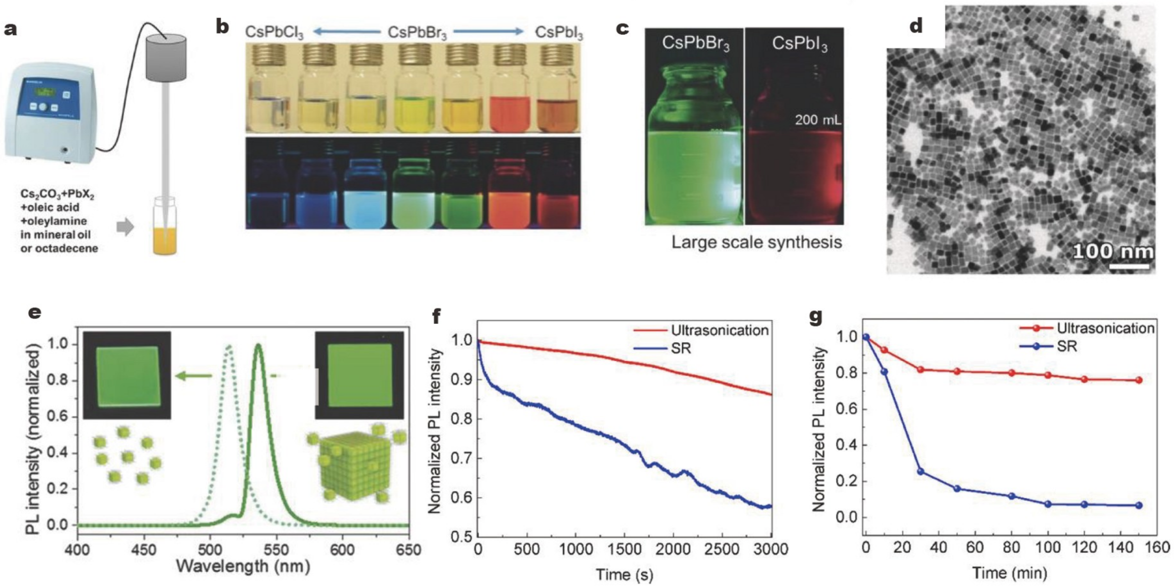

Figure 7 (a) Schematic representation of one-step tip sonication synthesis; photographs of (b) halide substitution reaction, and (c) large-scale synthesis; (d) TEM image of CsPbBr$_3$. Reprinted with permission from Ref. [48], Copyright 2016, Wiley-VCH Verlag GmbH &Co. (e) PL spectra of individual and supercrystals. Reprinted with permission from Ref. [62], Copyright 2018, WILEY-VCH Verlag GmbH & Co. KGaA, Weinheim. (f) Photostability of CsPbBr$_3$ NCu colloidal solution under 365 nm continuous excitation; (g) thermostability of CsPbBr$_3$ NCu film at 80°C, synthesized by US (red) and at room temperature (blue). Reprinted with permission from Ref. [61], Copyright 2018, American Chemical Society.

(Fig. 7d), exhibiting redshifted PL due to electron coupling caused by self-assembling (Fig. 7e) [62]. Rao *et al.* [61] demonstrated the possibility of morphology and size control *via* capping ligands, ultrasound power (90–120 W), and reaction time adjustment, leading to the NCus, NPLs, NWs, and QDs. In another study, MHP NCus expressed enhanced photo- and thermo-stability (Fig. 7f, g) compared with NCs synthesized by the room-temperature LARP method, due to hydrophobic liquid paraffin used as a solvent, which protects the NC surface from moisture, oxygen, and halogen hydrogen bonding from oxidation. Moreover, US can control phase transformation, i.e., Cs$_4$PbBr$_6$ could be prepared using an excess of OAm under 40-minute-US at 90 W [61]. It was also denoted that the immersion height of the tip should not exceed more than 20% of the total liquid height for the best PLQY effect [105]. The US method allows the preparation of MHPs in polar alcohols such as butanol [106].

Solvothermal synthesis

The SV process is a fast and simple method aiming at dissolving precursors in a reactive medium and growing MHPs at elevated temperature and pressure. The pre-treatment of precursors (CsOAc, PbX$_2$, OAm, OA and ODE) before the reaction directs the morphology of MHPs. In the case where non-pre-treated precursors are inserted in the autoclave and heated up to 160°C for 30 min under air, CsPbBr$_3$ and CsPbI$_3$ NCus are obtained with sizes of 8.2 and 12.5 nm, respectively (Fig. 8a–e). Pre-dissolving precursors in ODE yields orthorhombic green emitting CsPbBr$_3$, blue emitting CsPb(Br/I)$_3$, and CsPb(Cl/Br)$_3$ NWs with strong quantum confinement (Fig. 8f–h) [66]. Zheng's group [68] demonstrated the formation of CsPbX$_3$ NPLs and NSs through the self-assembly of NRs. The thickness was controlled

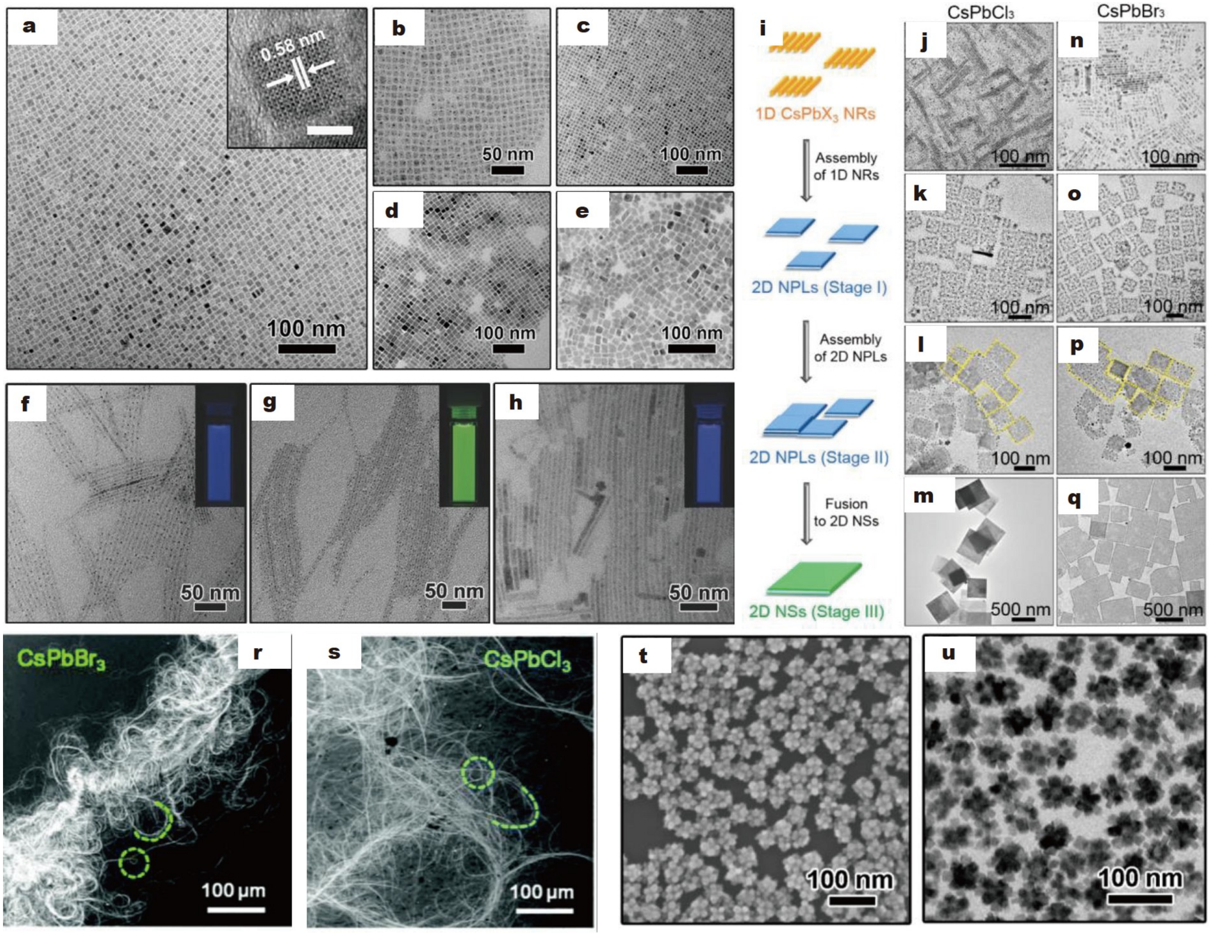

Figure 8 Morphology analysis of MHP materials. (a) TEM images of $CsPbBr_3$ (inset: HRTEM; the scale bar is 5 nm.), (b) $CsPbCl_3$, (c) $CsPb(Cl/Br)_3$, (d) $CsPb(Br/I)_3$ and (e) $CsPbI_3$ NCus, (f) $CsPbBr_3$, (g) $CsPb(Br/I)_3$, and (h) $CsPb(Cl/Br)_3$ ultrathin NWs, with $CsPbX_3$ solution in hexane excited under UV illumination (λ = 365 nm) (insets). Reprinted with permission from Ref. [66], Copyright 2017, WILEY-VCH Verlag GmbH & Co. KGaA, Weinheim. (i–q) Synthesis scheme and TEM images of $CsPbBr_3$ and $CsPbCl_3$ NPLs and NSs obtained through self-assembly of NRs. Reprinted with permission from Ref. [68], Copyright 2018, American Chemical Society. (r, s) SEM images of ultrathin $CsPbB_3$ and $CsPbCl_3$ NWs with ultra-high aspect ratios. Reprinted with permission from Ref. [65], Copyright 2018, The Royal Chemical Society. (t, u) SEM and TEM images of $CsPbBr_3$ nanoflowers. Reprinted with permission from Ref. [69], Copyright 2018, Elsevier Ltd.

up to 1 μm by reaction time and mixing of long- and short-chain ligands, under an inert atmosphere at 160°C. The final MHPs displayed a relatively low PLQY of 20% (Fig. 8i–q).

Apart from NR self-assembling, NPLs with outstanding tunable lateral size can be synthesized by varying either the temperature (60–180°C) or reaction time, providing NPLs with either extended or reduced lateral size, respectively [64]. It is worth noting that in both cases the NPL thickness remains constant (~4.2 nm) [64].

The impressive $CsPbB_3$ and $CsPbCl_3$ NWs with ultra-high aspect ratios could be obtained at 100°C (72 h), when using pre-dissolved PbX_2 and Cs_2CO_3 as precursors, exhibiting PLQY of 75% (Fig. 8r, s) [65]. The SV method provides the possibility of designing nanoflowers under an inert atmosphere at 120°C, through the seed-mediated mechanism, with PLQY of 50% (Fig. 8t, u) [69]. The mechanism of nanoflower synthesis considers the formation of rhombohedral Cs_4PbBr_6 seeds in a Cs-rich environment at the very beginning of the reaction due to faster dissolution of CsOAc than $PbBr_2$, following the complete transformation to the cubic $CsPbBr_3$ after 30-minute-long reaction. The SV method offers one-step synthesis providing NCs with versatile morphologies. However, it can be time-consuming compared with the previously described methods. Even though some reports present SV as a large-scale method, it is limited by the reactor volume, and it does not provide more than 0.2 g per batch of synthesis.

Green synthetic procedures

The development of green synthetic procedures is an essential step for scaling up MHP production. Such methods usually consider either solvent-free reactions, i.e., solid-state reactions, or green solvent approaches. Finding a perfect eco-friendly procedure is an onerous task, and certain compromises must be taken into account, e.g., solvent-free synthesis requires considerable energy consumption and an inert environment. Ng *et al.* [107] adapted the LARP method by replacing toluene and OAm with ethyl acetate and octylamine, respectively. This approach reduces solvent waste by 62.5% and total ligand concentration by 60%, with an astonishing yield of 70% per reaction. Liu *et al.* [77] reported the green solvent synthesis of $CsPbBr_3$ NCs in water, using an organic building block, 2-methylimidazole (MEIM). The organic layer helps coordination chemistry by

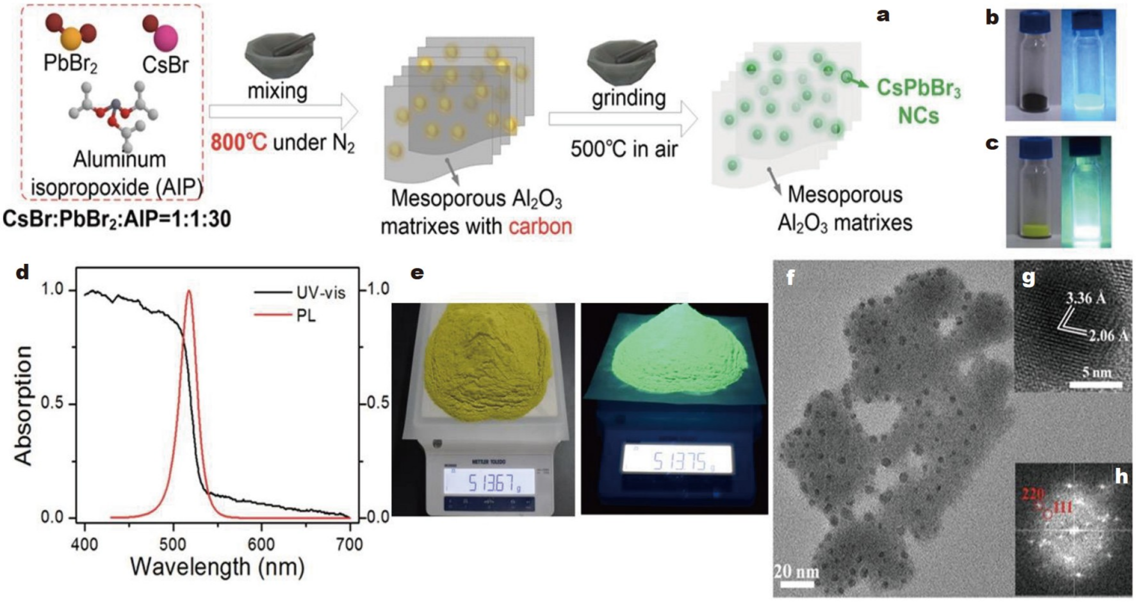

Figure 9 Large-scale production of CsPbBr$_3$@Al$_2$O$_3$ powder. (a) Schematic representation of the high-temperature solid-state reaction synthesis; (b) photograph of black powders after calcination under nitrogen atmosphere; (c) photographs of final products after annealing under an ambient atmosphere; (d) absorption and PL spectra; (e) photography of CsPbBr$_3$@Al$_2$O$_3$ powder; (f) TEM image of CsPbBr$_3$@Al$_2$O$_3$; (g) HRTEM image of one individual CsPbBr$_3$ NC, and (h) the corresponding fast Fourier transform image. Reprinted with permission from Ref. [78], Copyright 2019, American Chemical Society.

absorbing metallic precursors, favoring NC synthesis. The ground PbX$_2$ and CsBr are immersed in MEIM aqueous solution and stirred for 3 h. In such a way, CsPbBr$_3$/MEIM NCs of 8–10 nm in diameter were formed, displaying excellent photostability.

Wang *et al.* [78] reported the solid-state preparation of thermally stable CsPbBr$_3$ embedded in Al$_2$O$_3$ mesoporous matrixes, by mixing CsX, PbX$_2$, and Al-isopropoxide (AIP), followed by annealing at 800°C for 10 min under nitrogen atmosphere (Fig. 9a). The carbonization of AIP at 800°C produces a substantial amount of carbon, permitting MHP stability preservation. Subsequently, decarbonization is performed by calcination at 500°C under an ambient atmosphere, achieving yellow CsPbBr$_3$@Al$_2$O$_3$ NCs. Without any purification, NCus could be achieved with a high PLQY of 70% (Fig. 9b–d). Moreover, 500 g of CsPbBr$_3$@ Al$_2$O$_3$ could be obtained per one synthesis batch (Fig. 9e), being well crystallized, but not quantum-confined (Fig. 9f–h). The green and sustainable synthesis of MHPs could also be advanced through the contribution of machine learning and robot-based high-throughput screening (HTS), i.e., automated synthesis [108,109].

Post-synthetic reactions and their influence on MHP's optical properties

Different synthetic pathways yield cubic CsPbBr$_3$ NCs; however, PLQYs and lifetimes experience certain discrepancies. It is worth noting that purification has an important influence on PL [79].

The origin of the excellent optical properties of MHP lies in its intrinsic defect-tolerant electronic structure, stemming from the lack of bonding-antibonding interactions between conduction band (CB) and valence band (VB) [110]. According to simulations by Kang *et al.* [110], the majority of intrinsic defects correspond to the shallow trap states, which do not contribute dramatically to the non-radiative recombination, rendering MHPs as highly defect-tolerant semiconductors with high PLQY (>90%) and suppressed PL blinking [111]. Moreover, they demonstrated that Br-rich conditions introduce high defect concentrations, whereas moderate or Br-poor condition increases the energy formation of Cs, Br, and X vacancies, interstitial and antisite defects above 1 eV [110]. Hence, when choosing synthetic conditions, one should refer to these findings in order to obtain high PLQYs and long PL lifetimes.

Herein, we will discuss various post-synthetic procedures and their influence on MHP's structural, morphological, and optical properties. Besides direct ionic exchanges, the presence of secondary phases such as Cs$_4$PbBr$_6$, and surface coating of MHPs could have a drastic impact on the optical properties of MHPs.

Anion exchange reactions have introduced an easy and rapid way of tuning MHP stoichiometry and the optical bandgap energy. Possible exchange reactions are Cl–Br–I or I–Br–Cl, but Cl/I perovskite cannot be obtained due to the difference in the atomic radii. Kovalenko and Manna's groups [39,112] were the first to report anion exchange upon MHP synthesis. Kovalenko's group [39] used PbBr$_2$, PbI$_2$, OAmX, and MeMgX as the anion sources previously dissolved in ODE at a higher temperature, and then kept at 40°C, followed by injection of MHP dispersed in toluene (particle size ~10 nm). Manna's group [112] reported room-temperature anion exchange using methylammonium bromide (MA-Br), octadecylammonium halides (ODA-X), OAmX, and tetrabutylammonium iodide (TBA-X) (particle size ~8–9 nm) (Fig. 10). Mandal's group [51] reported anion exchange with HCl and HI acids diluted in DMF (particle size ~11 nm). It should be noted that precursors with MA's group could trigger Cs substitution, hence they should be avoided if the exchange of A cation is not the aim.

Despite the values varying from one direct method to another, they are very similar in proving unambiguously dramatic decay of PLQY with Cl prevalence in the structure, while Br/I mixtures

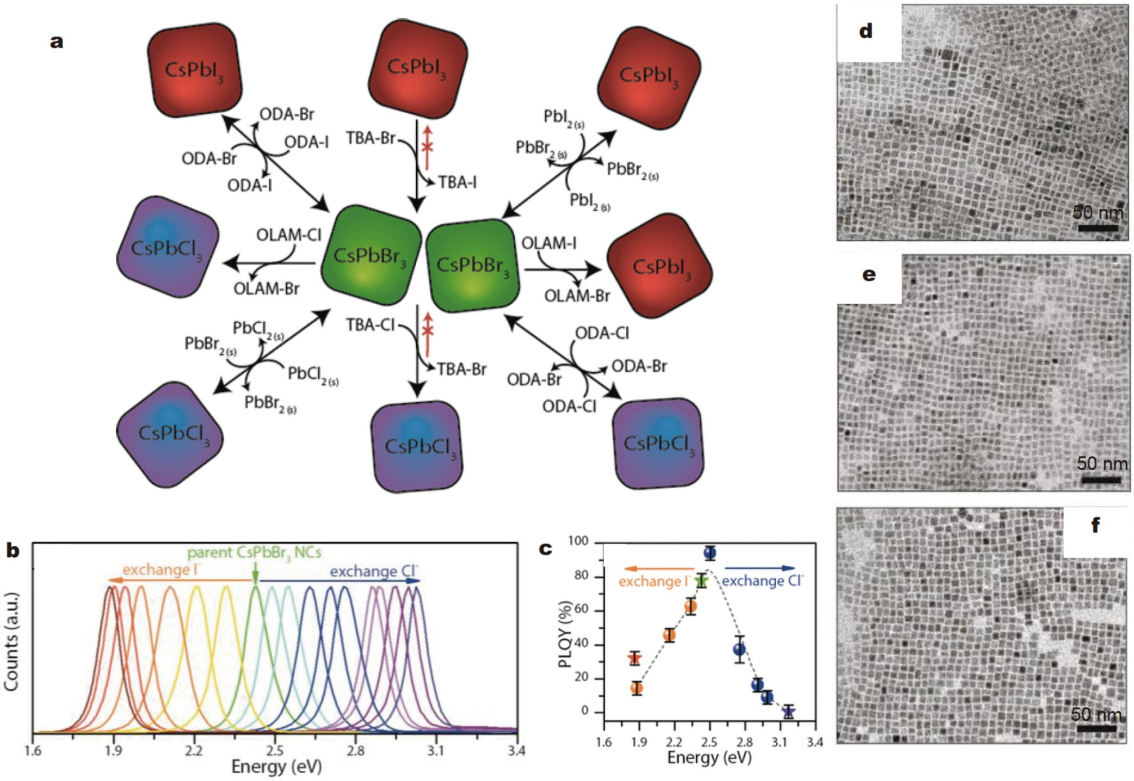

Figure 10 (a) Schematic of anion exchange at room temperature with different precursors; (b) PL spectra of anion exchanged NCs; (c) PLQY recorded on the exchanged NCs (dots) as well as on the directly synthesized NCs (stars), TEM images of (d) the anion exchanged $CsPbBr_{3-y}Cl_y$, (e) pristine $CsPbBr_3$ NCs, and (f) anion exchanged $CsPbBr_{3-y}I_y$. Reprinted with permission from Ref. [112], Copyright 2015, American Chemical Society.

express higher PLQY than pure $CsPbBr_3$, finally resulting in a high quantum yield for pure $CsPbI_3$ [59,60]. However, anion exchange at room temperature demonstrated dramatic decay of PLQY, upon exchange of bromine with both chloride and iodine (Fig. 10c) [112], while anion exchange at 40°C retained high quantum yields comparable to the direct synthesis [39].

Cation exchange reaction of Cs with MA was recognized in the above-mentioned reaction when MABr was used as a precursor for anionic exchange. Substitution of Cs with organic moieties such as MA or formamidinium (FA) could be easily achieved; however complete substitution of B cation leads to distortion of PbX_6 octahedra and cubic crystal lattice. Partial substitution of Pb appeared to be successful, and it was achieved by metal bromide salts (MBr_2, M = Sn^{2+}, Zn^{2+}, and Cd^{2+}) dissolved in toluene in the presence of OAm, with preservation of the pristine size and shape (Fig. 11a–e), the main disadvantage of this method is a lack of MHP precipitation [52]. Partial substitution of Pb with divalent cations Sn^{2+}, Zn^{2+}, and Cd^{2+} allows tuning of PL from 452 to 512 nm, with PLQY over 60%, due to the change in the electronic structure upon creation of a shorter Pb–halide bond (Fig. 11d, e). Such lattice distortion leads to stronger interactions between Pb and halide orbitals, and consequently to the increased MHP band gap. It is worth noting that in the case of Sn^{2+} partial substitution, observed PL and absorption fingerprints stem from $PbBr_6$, while the additional absorption band in the red region corresponds to $SnBr_6$ octahedra (Fig. 11d) [52]. It is well known that $CsPbCl_3$ suffers from very low PLQY being less than 10%, whereas doping with Cd^{2+} drastically enhances its PL features while keeping PL peak position and spectral width (Fig. 11e) [113].

Further MHP doping was achieved with Cu^{2+}, Ni^{2+} or Co^{2+}, resulting in PL enhancement (Fig. 11f–i) [40–44,53–55]. Interestingly, nickel and copper at excessive dopant concentrations lead to PL quenching (Fig. 11g, i) [44,54]. Such behavior indicates non-radiative electron transfer that could enhance the charge-carrier separation, allowing efficient photocatalytic reactions. Doping of $CsPbCl_3$ NCus and $CsPbBr_3$ NPLs with Mn^{2+} causes the appearance of a new PL band in higher energy region, at ambient conditions (Fig. 11j, k) [59,114,115], while $CsPbBr_3$ NCus experience such emission only below 225 K (Fig. 12f) [116].

Apart from divalent doping, MHP could be modified by trivalent cations, i.e., Al^{3+}, Ce^{3+}, or Bi^{3+}. A density functional theory (DFT) study demonstrated that Ce^{3+}/Bi^{3+} occupy either Pb^{2+} anti- or interstitial sites in the MHP host lattice, at Br rich/moderate or poor condition, respectively (Fig. 12a–c) [46]. The Bi_{Pb} antisite has a transition level energy at 0.59 eV and interstitial Bi_i at 0.7 eV below CB minimum (CBM), while Ce_{Pb} and Ce_i transition levels are located at 0.2 eV below CBM for both orthorhombic and cubic MHP hosts. These transition levels are known as the deep and shallow trap states introduced through the doping [46]. Ce^{3+} shallow traps improved PLQY, which evolved from 41% to 89%, without influencing defect-tolerant properties [45–47]. On the contrary, doping with bismuth negatively affects PL due to the formation of the deep trap states (Fig. 12d, e) [46]. The Ce^{3+} and Bi^{3+} doping leads to the formation of shallow and deep traps, respectively. The formation of a shallow trap enhances the PL, which translates to higher

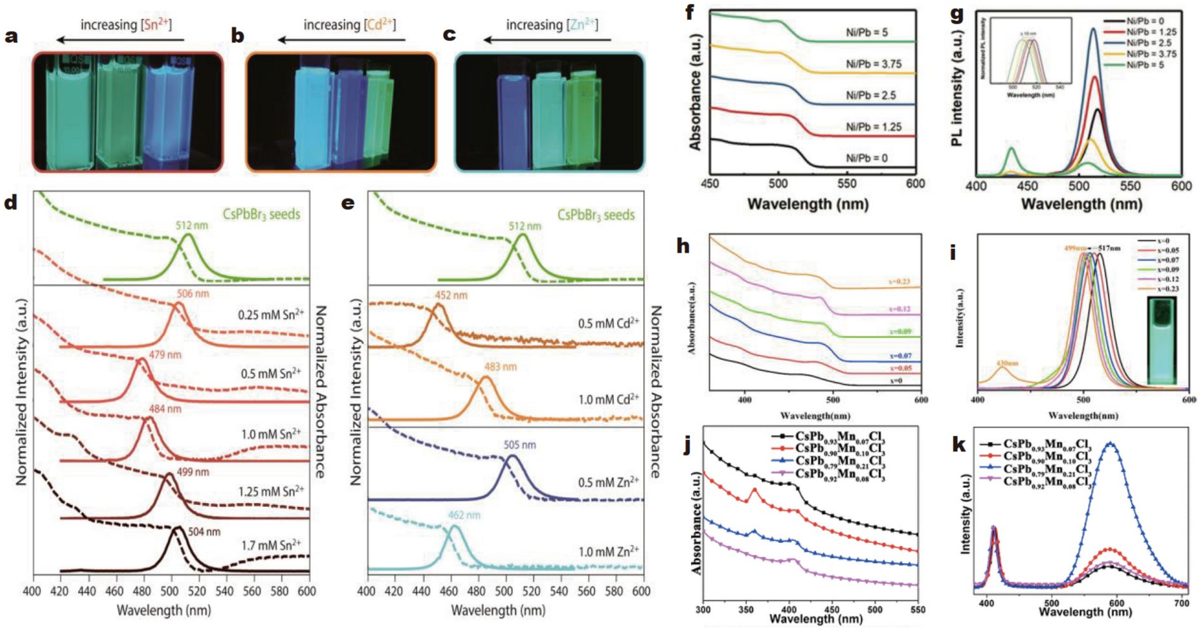

Figure 11 MHP doped with different transition metals, and their PL responses. (a–e) Partial substitution of Pb with Sn, Zn, and Cd in $CsPbBr_3$. Reprinted with permission from Ref. [52], Copyright 2017, American Chemical Society; (f, g) $CsPbBr_3$ doped with Ni^{2+}. Reprinted with permission from Ref. [44], Copyright 2021, Wiley-VCH GmbH; (h, i) $CsPbBr_3$ doped with Cu^{2+}. Reprinted with permission from Ref. [54], Copyright 2019, American Chemical Society, and (j, k) $CsPbCl_3$ doped with Mn^{2+}. Reprinted with permission from Ref. [59], Copyright 2017, American Chemical Society.

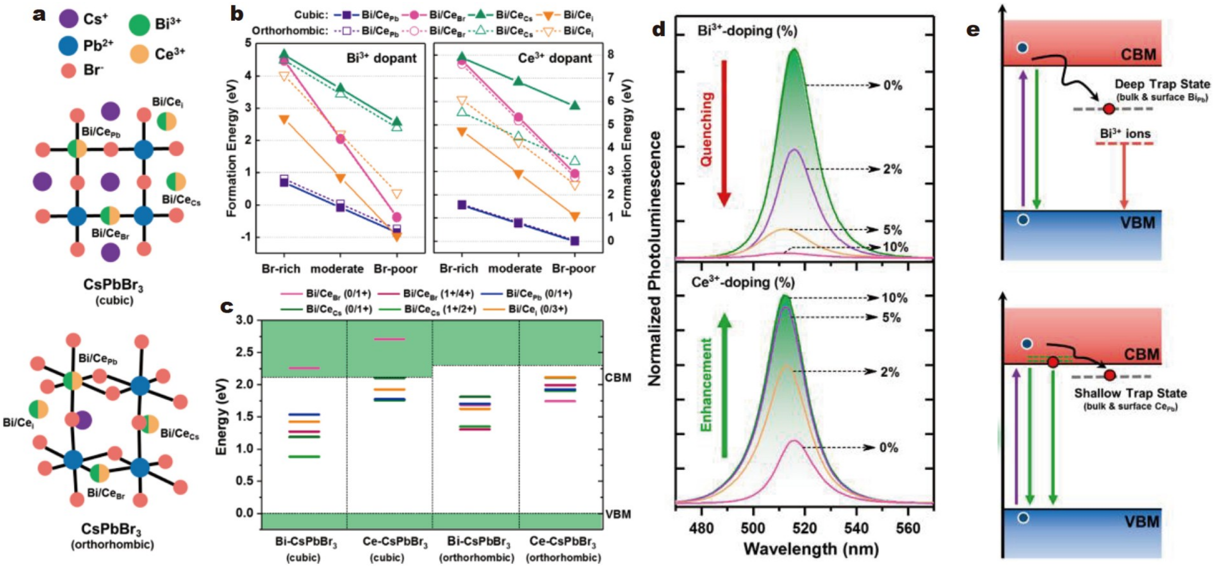

Figure 12 (a) Schematic representation of the cubic and orthorhombic $CsPbBr_3$ crystal phases with Bi^{3+} and Ce^{3+} dopants at Cs, Pb, and Br sites (Bi/Ce_{Cs}, Bi/Ce_{Pb}, and Bi/Ce_{Br}) and with Bi^{3+} and Ce^{3+} interstitials (Bi/Ce_i); (b) calculated doping formation energies, and (c) doping charge-transition levels for Bi/Ce_{Cs}, Bi/Ce_{Pb}, Bi/Ce_{Br}, and Bi/Ce_i in cubic and orthorhombic $CsPbBr_3$ crystal phases (Heyd–Scueria–Ernzerhof hybrid functional (HSE) + spin-orbit coupling (SOC) level of theory); (d) normalized PL spectra of $CsPbBr_3$ NCs upon Bi^{3+} and Ce^{3+} doping (2, 5, and 10 mole%); (e) schematic representation of energetic diagrams depicting the PL quenching/enhancing process in Bi^{3+}-doped and Ce^{3+}-doped $CsPbBr_3$. Reprinted with permission from Ref. [46], Copyright 2019, American Chemical Society.

recombination of photogenerated e^-/h^+, which could be detrimental to photocatalytic reactions. However, Bi^{3+} doping generates a deep trap that lowers the charge carrier recombination, and induces a PL quenching and longer e^-/h^+ lifetime, which could lead to improved photocatalytic efficiency. In contrast, the same group reported that defects created in the $CsPbBr_3$ using *in situ* Bi^{3+} doping using a hot-injection strategy lead to the formation of shallow defects (also known as trap states) with no modification of the bandgap structure [117]. The invalidity of the bandgap engineering using Bi^{3+} doping was also reported by Miyasaka's group [47], indicating the formation of localized states. Further doping with aluminum results in blue-shifted luminescence of $CsPbBr_3$ and $CsPb(Br/I)_3$, with PLQY and PL lifetime being significantly decreased [118].

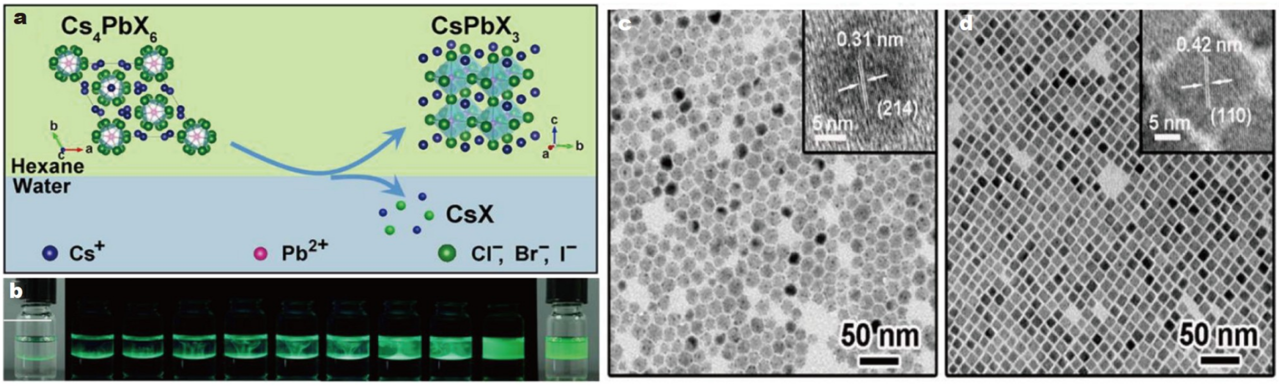

Figure 13 (a) Schematic representation of crystal structure and transformation process from Cs_4PbX_6 to $CsPbX_3$ upon water treatment. (b) Colloidal solutions of Cs_4PbX_6 to $CsPbX_3$ in hexane under UV illumination (λ = 365 nm) during transformation. TEM and HRTEM (insets) images of (c) Cs_4PbBr_6 and (d) $CsPbBr_3$ NCs. Reprinted with permission from Ref. [74], Copyright 2017, American Chemical Society.

Post-conversion of Cs_4PbX_6

The synthesis of Cs_4PbX_6 is very similar to the hot injection method. Cs and Pb salts, together with OAm and OA, are dissolved in ODE at 150°C and then cooled down to either 80, 100, or 60°C for $PbBr_2$, $PbCl_2$, and PbI_2, respectively. Then Cs-oleate is quickly injected, and the reaction mixture becomes white. Depending on the desired size, the reaction is quenched by immersion in an ice-water bath for 0–10 min. In order to obtain MHPs, 0D Cs_4PbBr_6 is dispersed in toluene, and a solution of $PbBr_2$ is injected, leading to the formation of the $CsPbBr_3$ [72]. The same quenching principle can be applied in SV reaction for the preparation of $CsPbBr_3$ NPLs, but also, Cs_4PbX_6 can be prepared by treatment of $CsPbBr_3$ with CsX [64]. MHPs can be also obtained upon calcination of Cs_4PbX_6 at 150–250°C; however, conversion is not complete. It is rather a reaction with Prussian blue in a solution that succeeds full conversion [73], and water-triggered conversion in a two-phase hexane/water solution that yields MHPs (Fig. 13a) [74]. Due to the surface decorated with OH groups, the stability and PL properties of $CsPbBr_3$ are improved (Fig. 13b–d).

The co-existence of the secondary phase significantly alters the PLQY of MHPs, although the origin of Cs_4PbBr_6 green emission remains unclear. It is widely accepted that the green emission is a consequence of $CsPbBr_3$ traces; however, some studies are claiming defect-induced emission originates either from Br vacancies, polybromide, self-trapped excitons, or interstitial hydroxyl [9]. According to Wang *et al.* [9], there should be three different distinguished types of Cs_4PbBr_6-based materials: pure UV-active non-emissive Cs_4PbBr_6 (P-Cs_4PbBr_6), defective-Cs_4PbBr_6 (D-Cs_4PbBr_6), and $CsPbBr_3$/Cs_4PbBr_6 hybrid (H-Cs_4PbBr_6), depending on their different structural and PL properties. We will not focus on the intrinsic photoluminescent properties of Cs_4PbBr_6, but on its influence on charge carrier dynamics of $CsPbBr_3$. The impact of Cs_4PbBr_6 on PL can be understood through the temperature-dependent PL measurements (Fig. 14a–d) [119]. In the temperature range of 300 to 77 K, pure $CsPbBr_3$ films exhibit improved PL intensity as expected in such conditions: lower vibrational population in the crystal lattice results in less phonon–electron interactions, allowing recombination of charge carriers (Fig. 14e). The presence of Cs_4PbBr_6 impurities gives rise to the shallow trap states near the CB band (Fig. 14f), which could be only thermally activated, leading to enhanced PL lifetime (Fig. 14g). These states are considered shallow since the minimum ionization energy, k_bT, needed for the electron de-trapping, is achieved at the ambient temperature.

Encapsulation of MHPs

MHPs undergo severe damage due to the high sensitivity to moisture when submitted to UV light, and they need to be protected from a highly humid environment [120]. A significant improvement of the MHPs' stability has been achieved by crosslinking C=C double bond structure [48], organic ligands [19,121], and polymer matrices [122], forming a hydrophobic coating. Thermal and humid resistance of $CsPbI_3$ was also achieved by Br doping and phenyltrimethylammonium organic cation surface passivation, leading to enhanced efficiency conversion [123]. Other strategies aimed at encapsulating MHPs in graphene oxide (GO), SiO_2, TiO_2, and AlO_x, forming a protective shell [124–132]. The core-shell nanostructure showed higher stability in a humid environment. The TiO_2 shell coating was also proposed as a protective layer for the MHPs, exhibiting improved chemical stability, and remarkable (photo)electrochemical properties [131].

The encapsulation of $CsPbBr_3$ with different amorphous metallic oxides MO_2 (M = Ti, Si, Sn) allowed greater stability of MHPs while preserving their morphological and structural properties [130,132–134]. Encapsulation does not impact absorption spectral lines, except the SnO_2 coating layer that causes a blue shift in both absorption and PL spectra due to the chloride impurities in the commercially available SnO_2 precursor, forming $CsPbBr_{1-x}Cl_x@SnO_2$ (Fig. 15a–d) [134]. This approach enables a simultaneous core@shell structure design and optical band gap tuning. The shell is usually amorphous with a thickness of 1–3 nm (Fig. 15e–h). Due to the CB and VB alignment of SnO_2, TiO_2, and MHP, electron transfer from MHP to metallic oxide is possible, resulting in the PLQY reduction from 37% to 7% (TiO_2) and 3% (SnO_2) [133]. Silica acts as an insulating layer enhancing the radiative recombination and PL emission intensity, resulting in a quantum yield of 64% *versus* 37% for pristine $CsPbBr_3$. The reason behind such PL improvement lies in surface defect passivation. Besides amorphous MO_2 layers, attempts to encapsulate MHP in crystalline TiO_2 were successful (Fig. 15j, k). A core@shell crystalline

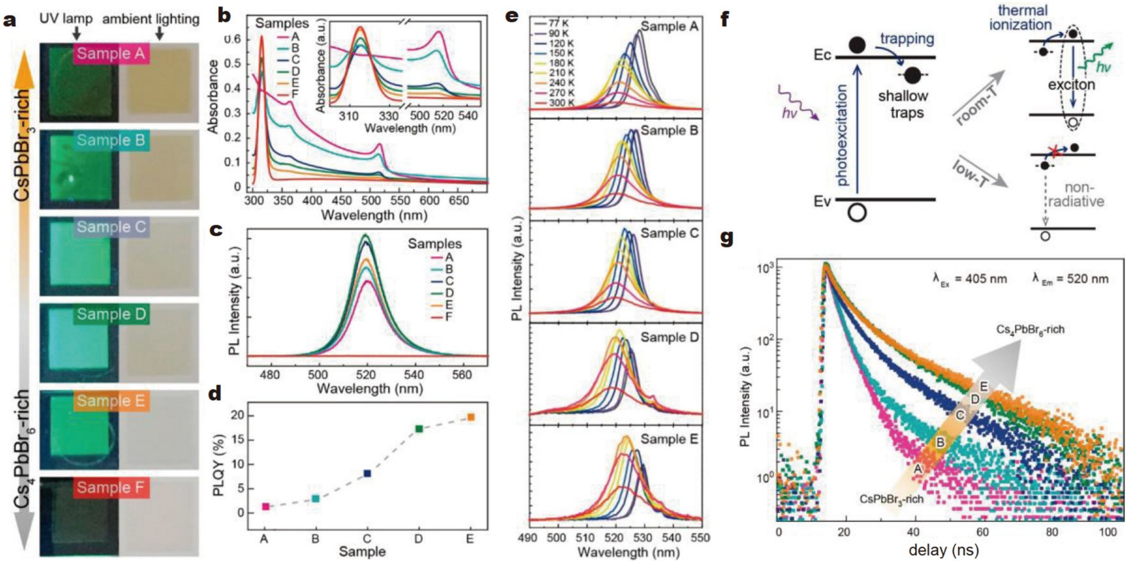

Figure 14 (a) Thin films of $CsPbBr_3$ with the increasing amount of Cs_4PbBr_6 (samples A–F); (b) absorption; (c) PL spectra; and (d) maximum PLQY for samples A–F; (e) temperature-dependent PL; (f) schematic representation of trapping mechanism; (g) PL decay for samples A–F. Reprinted with permission from Ref. [119], Copyright 2017, American Chemical Society.

structure formed upon calcination at 300°C under argon displayed enhanced stability (Fig. 15l–n) as well as superior photoelectrochemical properties [131].

CHARGE-CARRIER LIFETIME: TRANSIENT ABSORPTION SPECTROSCOPY (TAS), TIME-RESOLVED PL (TRPL), AND TIME-RESOLVED MICROWAVE CONDUCTIVITY (TRMC)

The long carrier lifetime and long diffusion lengths exceeding to micro-scale are rendering MHP perfect for photovoltaics and photocatalytic reactions, where charge carrier separation is pivotal [135–137]. Hence, substantial research on MHP's photophysics has been conducted to understand the excited state, trapping, and recombination dynamics, by means of various techniques such as TAS, TRPL [138], time-resolved terahertz spectroscopy (TRTS) [139–141], TRMC [142,143], and 2D electronic spectroscopy (2DES) [26].

Ultrafast spectroscopy, i.e., TAS, is focused on the exciton dynamics and many-body interactions, i.e., biexciton effect, state filling, and Auger non-radiative recombination. TAS also provides information on carrier–phonon interactions, charge-carrier trapping, and exciton radiative recombination, further being complemented with TRPL. Charge-carrier diffusion and mobility could be investigated by techniques such as 2DES, TRTS, and TRMC. Along with previously mentioned experimental techniques, molecular simulation studies provide complementary information on carrier–carrier and carrier–phonon interactions [144].

Ultrafast charge-carrier dynamics: TAS

TAS is a powerful tool for the investigation of rapid carrier processes due to its adaptable set-up (e.g., two pump excitation, pump-push-probe, and circular polarized probe beam) that allows differentiation of symmetric and asymmetric biexcitons, the role of cold carriers, and exciton spin relaxation lifetime, respectively [145–147]. In general, pump-probe measurements shed light on hot-carrier intraband cooling dynamics in fs time scale exceeding to pico- and nano-scale, discerning trapping and recombination processes while considering quantum confinement [148], cation and anion type [149,150], excitation energy and fluence dependence [151,152].

Typically, TAS of $CsPbBr_3$ obtained on above-band-edge using 350-nm excitation wavelength consists of photoinduced bleach (PB1), so-called ground state bleach (GSB), which corresponds to the bend-to-bend exciton transition (Fig. 16a, b). At early delay times ($\Delta t \leq 1$ ps), PB1 signal is redshifted (δ_{xx}) due to the formation of the biexciton [152]. Biexciton formation is a consequence of attractive Coulombic forces that bound two neutral excitons forming a biexciton [153]. Simultaneously with PB1, photoinduced absorption (PA2) at lower energies arises, representing a hot exciton cooling fingerprint, i.e., the intraband transition of the excited state (Fig. 16a, b). PA2 could also be a signature of bandgap renormalization (BGR) [148], and a polaron formation in thin films [154]. High energy tail (PB2) could be assigned to either BGR or hot exciton bleaching [152]. Photoinduced absorption above the bandgap (PA1) arises from forbidden exciton transitions in strongly confined MHP, and BGR in weakly confined/bulk MHP [151,155]. After Δt > 1 ps, redshift and PA2 disappear, and only symmetric pronounced bleach is observed, representing continuum bleach due to the state-filling effect.

High charge-carrier densities obtained at high excitation fluence (Fig. 16c, d) demonstrated BGR in weakly confined/bulk MHPs, observed as broadening (Fig. 16c) of the bleach signal (high-energy tail), and PA1 band at the longer delay (Fig. 16d), which are attributed to shifting in the density of states (DOS) upon BGR. Furthermore, high excitation fluences lead to slower charger-carrier relaxation due to the many-body interactions, i.e., non-radiative Auger recombination, phonon bottleneck, and polaron screening [151,154]. The right choice of the excitation energy successfully determines trapping processes in VB and CB discerning trapping states at low or high energy levels [152]. The

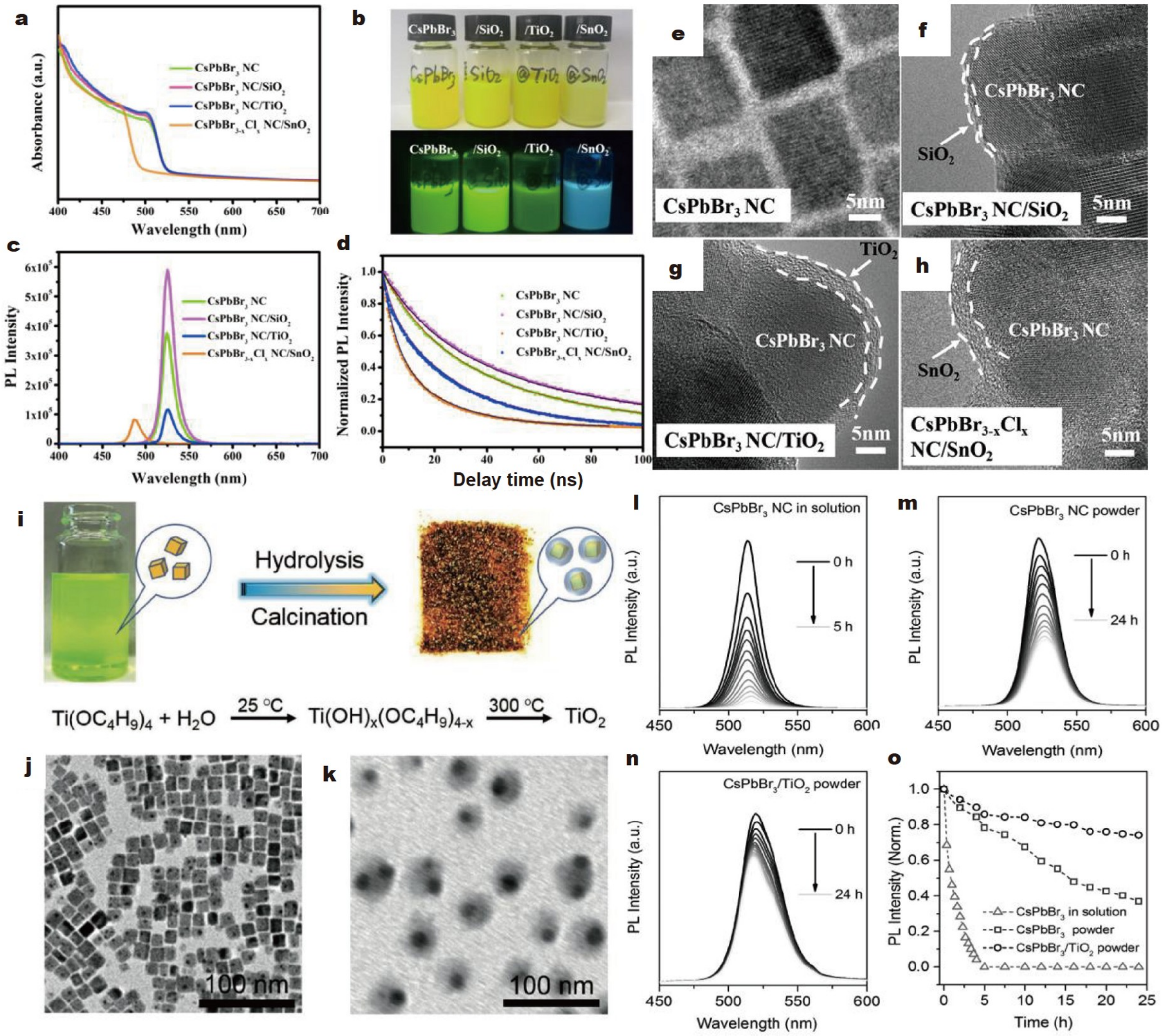

Figure 15 (a) UV-visible spectra; (b) sample photographs under daylight and UV light (λ = 365 nm); (c) PL spectra; and (d) TRPL decay curves of $CsPbBr_3$ NC, $CsPbBr_3$ NC/SiO_2, $CsPbBr_3$ NC/TiO_2, and $CsPbBr_3$ NC/SnO_2; (e–h) TEM images of $CsPbBr_3$ NC, $CsPbBr_3$ NC/SiO_2, $CsPbBr_3$ NC/TiO_2, and $CsPbBr_{3-x}Cl_x$ NC/SnO_2. Reprinted with permission from Ref. [133], Copyright 2018, American Chemical Society. (i) Schematic illustration of $CsPbBr_3$/TiO_2 core/shell NC synthesis; TEM images of (j) $CsPbBr_3$ NCs and (k) $CsPbBr_3$/TiO_2 core/shell NCs after calcination at 300°C for 5 h. Photostability of (l) $CsPbBr_3$ NCs in toluene, (m) $CsPbBr_3$ NCs powder, and (n) $CsPbBr_3$/TiO_2 NC powder under UV light by monitoring the relative PL intensity of the samples; (o) comparison of relative PL intensity for the three samples. Reprinted with permission from Ref. [131], Copyright 2017, WILEY-VCH Verlag GmbH & Co. KGaA, Weinheim.

effect of the quantum confinement on charge carrier dynamics appeared to be important only for very small NCs, resulting in a multimodal bleach shape (Fig. 16e), whereas weakly confined NCs (>7 nm) exhibit bulk-like photophysics [148]. Notably, the phonon bottleneck is independent of the size of NCs at higher excitation fluences [148]. Li *et al.* [156] did not observe any multimodal GSB shape for NCs <7 nm, on the contrary, they demonstrated exciton relaxation through a ligand-induced non-adiabatic relaxation mechanism in strongly confined $CsPbBr_3$, avoiding a hot bottleneck relaxation path.

A great deal of research was dedicated to investigating the influence of cations and anions on the excited state dynamics. Cs-based halide perovskites showed slower hot-carrier dynamics than organic halide perovskite due to the reduced effect of electron–phonon couplings due to less dominant interactions between Cs and PbX_6 octahedra [150,157]. Describing charge-carrier excited state dynamics upon anion substitution is more complex since the electronic values of the bandgap change. Chung *et al.* [149] demonstrated slower charge-carrier cooling upon partial substitution of bromide with iodide, possibly caused by the change of DOS, suggesting that holes might contribute mainly to hot carrier relaxation. Simultaneously, Mondal *et al.* [152] demonstrated the migration of holes from bromide to iodide, rendering iodide as a hole-trapping center. A partial substitution of Br with Cl has been quite investigated. However, the influence of Cl on charge carrier dynamics is still elusive. Soetan *et al.* [158] demonstrated that the addition of Cl affects a decrease in BGR energy leading to bandgap narrowing, larger exciton binding energy, and reduced Coulombic interactions. The addition of chloride resulted in a decreased Burstein-Moss effect compared with solely bromide-based MHP, which explains faster hot carrier cooling in mixed Br/Cl MHP. More-

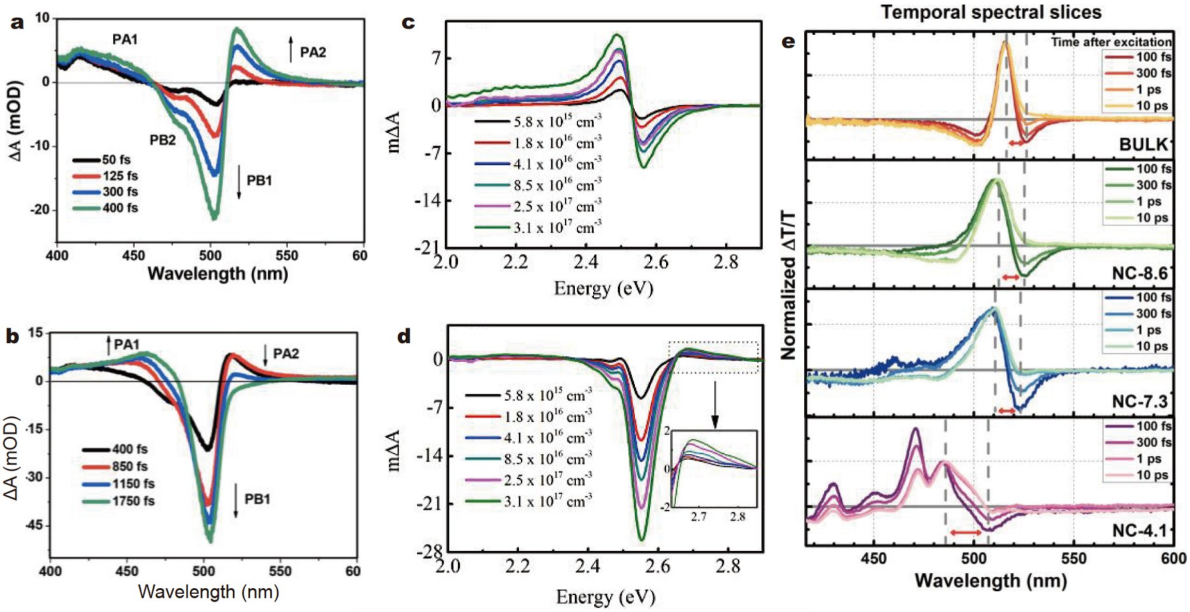

Figure 16 (a, b) Typical TAS of $CsPbBr_3$ obtained on above-band-edge using 350 nm excitation wavelength consisting of photoinduced absorption (PA1, PA2) and bleach (PB) at different delay times. Reprinted with permission from Ref. [152], Copyright 2017, The Royal Society of Chemistry. (c, d) Influence of excitation fluence. Reprinted with permission from Ref. [151], Copyright 2018, The American Physical Society. (e) Quantum confinement on spectral lines panel. Reprinted with permission from Ref. [148], Copyright 2017, American Chemical Society.

over, at higher pump fluences (13–80 μJ cm^{-2}), Auger recombination stands out as a dominant decay path, diminishing trapping assisted decay. In another study, Mandal *et al.* [159], at lower excitation fluences (<3 μJ cm^{-2}), assigned faster carrier cooling to the near band edge trapping states introduced upon insertion of chloride in the crystal structure.

To the best of our knowledge, ultrafast charge-carrier dynamics of doped MHPs have not been widely investigated, and there are only a few studies dealing with transient metal doping, such as Bi, Ni, and Mn [45,117,160,161]. MHP doping with bismuth results in the Burstein-Moss effect since the CB band is filled with additional electrons. Nanosecond TAS measurement showed slower bleach recovery (36 ns) compared with pure $CsPbBr_3$ (7 ns), implying a change in the electronic band structure that eventually leads to delayed carrier recombination. A slower intraband relaxation and more efficient charge transfer of doped MHPs in the presence of electron acceptors was observed by fs-TAS, due to the increase of Gibbs free energy ($-\Delta G$) [117]. Doping with nickel also slows down intraband relaxation, probably due to charge separation of the plasmon-MHP CB band, where hot electrons are transferred at the interface [162]. In the case of Mn-doped $CsPbBr_3$ NPLs, a strong competition was observed between energy transfer and electron transfer. The TAS reveals an additional bleach, energetically lower than band bleach, corresponding to the charge transfer, while PL studies describe energy transfer from NPLs to Mn at a picosecond time scale [161].

PL lifetime

PL lifetime is essential to understand MHPs' photophysics on pico- and nano-scale. As previously stated, the high-temperature synthetic procedure proved that the prevalence of chloride in MHP results in reduced PLQY and lifetime, whereas the presence of bromide and iodide enhances QY and PL lifetime (Fig. 17a) [19]. The MHPs obtained through high-temperature synthesis show drastically lower PL loss (10%) [138] when heated in the range of 80–273 K compared with MHPs synthesized through the LARP method at room temperature (85%) [70]. The average lifetimes calculated vary in different studies; note that NC purification substantially affects PL lifetime, ranging from 1 to 112 ns [19,60,82]. One should take into account the anion substitution method, since, at room temperature, PL quenching occurs even in the presence of iodide [112].

The most compelling way to investigate the PL of MHPs is through temperature-dependent PL, which provides valuable information on short and long PL lifetimes, giving insight into trap-assisted nonradiative and radiative recombination. Temperature-dependent PL measurements showed that Cl-based MHPs suffer from PL loss even at $T < 300$ K, while $CsPbBr_3$ and $CsPbI_3$ exhibited higher resistance up to $T = 450$ K (Fig. 17b) [138]. The extended PL lifetime for $CsPbBr_3$ and $CsPbI_3$ is attributed to surface reactions that mostly originate from halogen vacancies and surface defects. TRPL measurements proved that $CsPbBr_3$ expresses a short PL lifetime at $T > 400$ K, due to thermally introduced nonradiative pathways. PL loss appeared to be reversible up to 450 K. Once this temperature is exceeded (>450 K), the PL loss becomes irreversible. PL loss at elevated temperature could be due to increased anion mobility and ligand loss, which passivates the surface states.

Nenon *et al.* [163] evaluated the PLQY dependence on the concentration of surface halide defects in Br-poor conditions. Their findings showed that an increased concentration of halogen defects has little, moderate and substantial effects on the PLQYs of $CsPbI_3$, $CsPbBr_3$ and $CsPbCl_3$, respectively, meaning that the majority of defects originate directly from halide vacancies, since Pb vacancies would introduce the same effect to all $CsPbX_3$ NCs. Their *ab initio* calculations demonstrated that $CsPbCl_3$ consists of localized mid-gap traps that are responsible

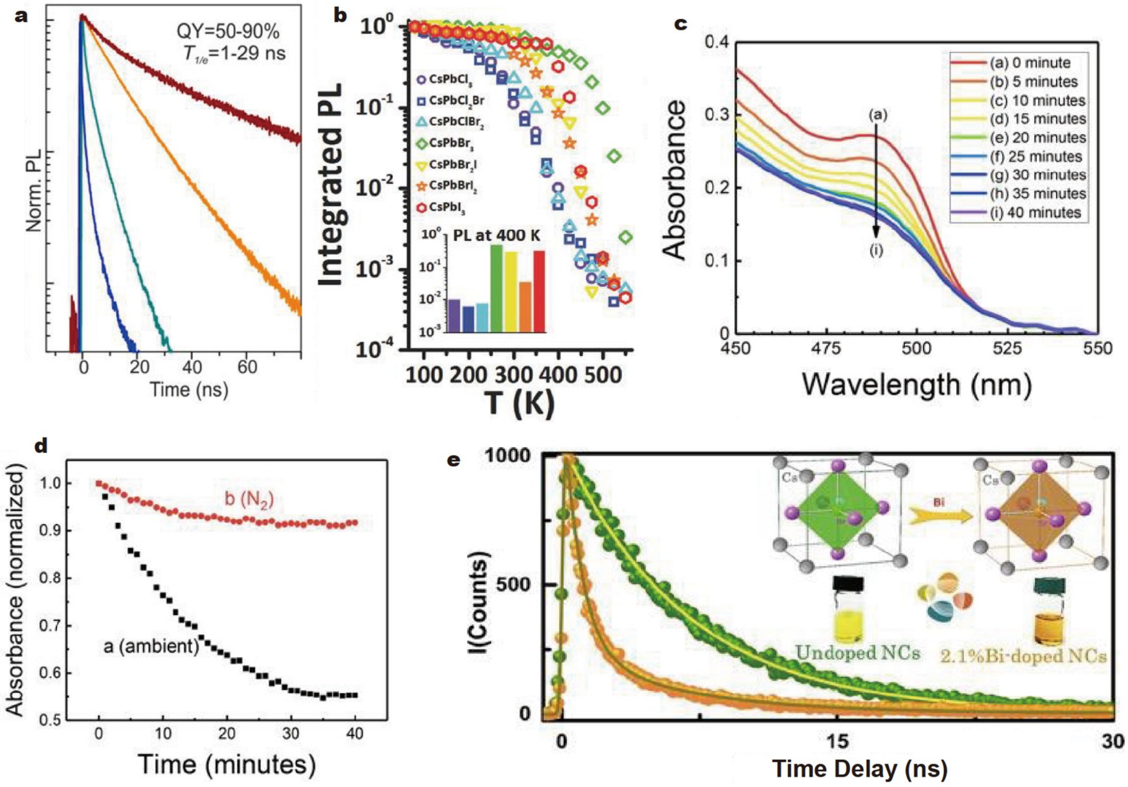

Figure 17 (a) TRPL lifetimes from $CsPbI_3$ (red), $CsPb(Br/I)_3$ (orange), $CsPb(Br)_3$ (cyan) to $CsPb(Br/Cl)_3$ (blue). Reprinted with permission from Ref. [19], Copyright 2015, American Chemical Society. (b) Integrated PL evolution of MHPs containing Cl, Br, and I at different temperatures. Reprinted with permission from Ref. [138], Copyright 2017, WILEY-VCH Verlag GmbH & Co. KGaA, Weinheim. (c) Absorption spectra of $CsPbBr_3/TiO_2$ films under white light continuous irradiation at ambient atmosphere; (d) normalized absorption of $CsPbBr_3/TiO_2$ recorded at 500 nm irradiated under ambient (black) and nitrogen (red) atmosphere. Reprinted with permission from Ref. [120], Copyright 2018, American Chemical Society. (e) TRPL lifetime decay of pristine $CsPbBr_3$ and Bi-doped $CsPbBr_3$. Reprinted with permission from Ref. [117], Copyright 2016, American Chemical Society.

for trap-assisted nonradiative recombination, while $CsPbBr_3$ and $CsPbI_3$ consist of slightly localized electrons and completely delocalized holes, resulting in higher PLQY. Surface passivation could enhance both PLQY and PL lifetime of $CsPbBr_3$ and $CsPbI_3$ through the exchange of hard oleate with soft carboxylates such as hexylphosphonate and benzoate, through the coordination of soft Pb binding sites with soft X-ligand carboxylates, while Cs vacancies are passivated with oleylammonium ligands. Hutter *et al.* [142] further investigated the mechanism of charge-carrier recombination in $CsPbI_3$ by means of temperature-dependent TRMC. The authors demonstrated that charge-carrier mobility and recombination dynamics in $CsPbI_3$ and $MAPbI_3$ are only limited by phonon scattering. In other words, MHPs' charge-carrier dynamics strongly depend on the PbI_6 framework, being completely independent of the A cation type. What is more, their findings indicate thermally enhanced second-order recombination, which could be a signature of an indirect recombination pathway.

Although the presence of chloride is considered non-beneficial for PL, it could slightly improve PL lifetime when added in small amounts to the mixed Br/I perovskite. In such a way, chloride becomes a lead defect (V_{Pb}) healer when added in small quantities, acting as a hole repellent, further reducing trapping and enhancing PL [164]. As previously stated, PL lifetime could be improved in the presence of Cs_4PbBr_6 impurities (Fig. 14), and by doping with different metals, such as Ni, Cu, Co, and Ce, that are discussed above. A more detailed discussion on the Cs_4PbBr_6 phase is given in the previous chapter and a detailed review by Wang *et al.* [9].

From the photocatalytic point of view, long-lived charge carriers are needed for optimal and efficient photochemical reactions. Assuming that the reactions occur at the μs scale, quenching the PL signal could be interpreted as a non-radiative phenomenon, thus beneficial for charge-carrier separation and their lifetime. PL lifetime could be manipulated through an adjusted synthetic approach previously discussed, i.e., room-temperature synthesis, multifaceted morphology, doping with metallic cations, and coating with appropriate semiconductors forming core@shell nanostructure [120,131]. In the case of coupling with TiO_2 as a semiconductor, the electron transfer from MHP to TiO_2 enhances charge-carrier separation. Interestingly, a thin TiO_2 layer could favor a *Z*-scheme electron transfer when optimal VBM and CBM are well adjusted, enhancing PL signal [9]. An efficient electron transfer occurs when nanostructures are excited under an inert atmosphere, avoiding electron capture by oxygen, which causes the accumulation of charges, leading to the corrosion of MHP (Fig. 17c, d) [120]. The MHP doping is another way of suppressing PL by directly influencing the electronic band structure. So far, one of the most interesting dopants is bismuth, which can significantly suppress PL even at very small amounts (Fig. 17e) [117]. In addition, PL lifetime can be diminished by Zn, Cd, Sn, Al doping and excessive amounts of Ni and Cu [44,52,55].

Charge-carrier diffusion lengths in $CsPbX_3$

MHPs are known for their long carrier diffusion length (L_D) exceeding >9.2 μm [139]. A direct study performed by scanning photocurrent microscopy (SPCM) on the single crystal of $APbX_3$ (A = MA, FA, Cs, X = Br, Cl, I) revealed that Cs-based halide perovskites experience L_D at the micrometer scale, however shorter than their organic counterparts. The diffusion lengths L_D decrease in the order MA > FA > Cs, where the difference between MA and Cs is 50%. Interestingly, unbalanced diffusion of electrons L_D^{e-} and holes L_D^{h+} in all $APbBr_3$ NCs appeared to be of one order of magnitude difference between L_D^{h+} (cc. 10–50 μm) and L_D^{e-} (cc. 1–5 μm) in $APbBr_3$ (A = MA, FA, Cs) NCs.

It is important to note that L_D^{h+} of $MAPbBr_3$ and $MAPbI_3$ do not depend strongly on the halide type, whereas L_D^{e-} are strongly dependent on anionic substitution. $MAPbBr_3$ experienced five times smaller L_D^{e-} and 1.3 times smaller L_D^{h+} than $MAPbI_3$. This behavior was confirmed by indirect TRMC measurements. These results are of great significance for the best choice of photocatalyst and solar cell efficiency [26].

PHOTOCATALYTIC APPLICATIONS OF MHPs

Designing an efficient photocatalyst with a suitable bandgap energy potential for hydrogen evolution remains a challenge. Hydrogen is considered as a promising chemical fuel, and studies are ongoing considering its production and storage [165–167]. Besides hydrogen production, CO_2 reduction, and degradation of organic molecules have been gaining tremendous interest in the photocatalytic community. The main obstacle to the employment of MHPs in photocatalysis is their inherent instability in polar solvents, and upon exposure to UV irradiation, which enhances the interactions between MHP (e.g., $CsPbBr_3$), CO_2, O_2, and H_2O, resulting in PbO formation (i.e., anodic corrosion) (Equations (5) and (6)) [168]:

$$2CsPbBr_3{\cdot}H_2O + 0.5O_2 + CO_2 \rightarrow 2CsBr + PbCO_3 + Pb(OH)_2 + 2HBr + Br_2, \quad (5)$$

$$Pb(OH)_2 \rightarrow PbO + H_2O. \quad (6)$$

The least stable cubic iodide-based MHPs (e.g., $CsPbI_3$) retain their structural properties only at temperatures above 645 K, and suffer from quick phase transition, resulting in a so-called yellow non-perovskite phase (δ-orthorhombic $CsPbI_3$ NCs), which limits their application [18,169,170]. In order to protect MHPs, a straightforward approach considers covering MHPs with a stable and robust overlayer, which would act as a barrier, preventing direct contact with the surrounding media, simultaneously allowing charge diffusion. What is more, polar medium can be substituted with either less polar or non-polar medium (e.g., ethyl acetate) allowing their wider application [171].

The photocatalytic performances of these materials have been intensively explored. The studies showed effective enhancement of the photocatalytic efficiency for CO_2 reduction when inorganic MHPs (e.g., $CsPbBr_3$) were coupled to GO titanium dioxide [132], zeolite [172], and $Re(CO)_3Br(dcbpy)$ (dcbpy = 4,4′-dicarboxy-2,2′-bipyridine) complex molecule as the active material [173]. The heterojunction improves the efficiency of charge-carrier photogeneration (i.e., electron–hole separation) and CO_2 capture. Mixed MHP $CsPb(Br_{0.5}/Cl_{0.5})_3$ demonstrated the effective removal of CO_2 from ethyl acetate saturated solution [171]. Several methods have been proposed to enhance the stability and, thus, the photocatalytic activity of MHPs for CO_2 reduction [97], H_2 generation [174], and toluene/ benzyl alcohol oxidation [175]. Herein, we will introduce some efficient strategies to boost the photocatalytic performance of MHPs, including surface and morphological modifications, doping with metals, and encapsulation with non-toxic and stable oxides such as TiO_2 and SiO_2.

Surface and morphological modifications of MHPs

Typically, $CsPbBr_3$ NCs are prepared by ionic metathesis, which considers the injection of Cs-oleate into the solution of $PbBr_2$ in OA, OAm, and ODE, at elevated temperature. In the preparation of metal-halide-perovskite NCs, capping ligands are indispensable for colloidal stability and shape control. However, long alkyl-chain capping ligands used in conventional MHP NCs synthesis (e.g., OAm and OA) are unfavorable for CO_2 adsorption, since they hinder the efficient carrier separation on the surface of MHP NCs and thus reduce the photocatalytic activity [81]. To meet these challenges, employing small organic molecules as capping ligands could be an ideal solution. Xu *et al.* [176] functionalized $CsPbBr_3$ NCs with short-chain glycine molecules ($CsPbBr_3$-Gly) and compared their photocatalytic performance in CO_2 reduction reaction (CO_2RR) with $CsPbBr_3$ NCs functionalized with long-chain OA and OAm ligands ($CsPbBr_3$-OA/OAm). $CsPbBr_3$-Gly NCs were prepared by simple ligand exchange of the as-prepared $CsPbBr_3$-OA/OAm upon adding to a saturated solution of glycine (Fig. 18a, inset). $CsPbBr_3$-OA/OAm NCs show a poor photocatalytic activity for CO_2 reduction in water, with CO formation rate of 4.8 $\mu mol\ g^{-1}\ h^{-1}$. However, $CsPbBr_3$-Gly NCs exhibit an excellent yield with CO generation rate of 27.7 $\mu mol\ g^{-1}\ h^{-1}$, being five times higher than that of $CsPbBr_3$-OA/OAm, with reproducible yields for three consecutive cycles. The enhanced photocatalytic performance of $CsPbBr_3$-Glycine NCs could be mainly attributed to the reduced hindrance of short-chain ligands, together with the strong interaction of glycine with CO_2 [176]. Moreover, replacing OA and OAm with glycine leads to a significantly higher photocurrent density compared with $CsPbBr_3$-OA/OAm NCs (Fig. 18b), demonstrating enhanced charge-carrier separation of $CsPbBr_3$-Gly. From the electrochemical impedance spectroscopy (EIS) Nyquist plots, one can observe a smaller semi-circle for $CsPbBr_3$-Gly, indicating significantly lower charge transfer resistance (Fig. 18c) [176].

The conventional OA could be also replaced by a shorter acetic acid, after the treatment of $CsPbI_3$ with methyl acetate. The obtained MeAc-$CsPbI_3$ proved to be more active in photocatalytic polymerization of 3,4-ethylenedioxythiophenereaction in nonpolar solvents (toluene and dichloromethane) than pristine $CsPbI_3$. The increase of photoactivity was attributed to an improvement in the charge transport, originating either directly from OA replacement or from introduced surface defects [177].

Morphology tuning is one strategy that has been proposed to improve the photocatalytic activity, assuming that the charge (e^-/h^+) separation and photocatalytic reactions are driven by the facet orientation. The multifaceted NCs could be an excellent strategy for efficient adsorption/desorption of reactants/products. NC morphology modification could increase the number

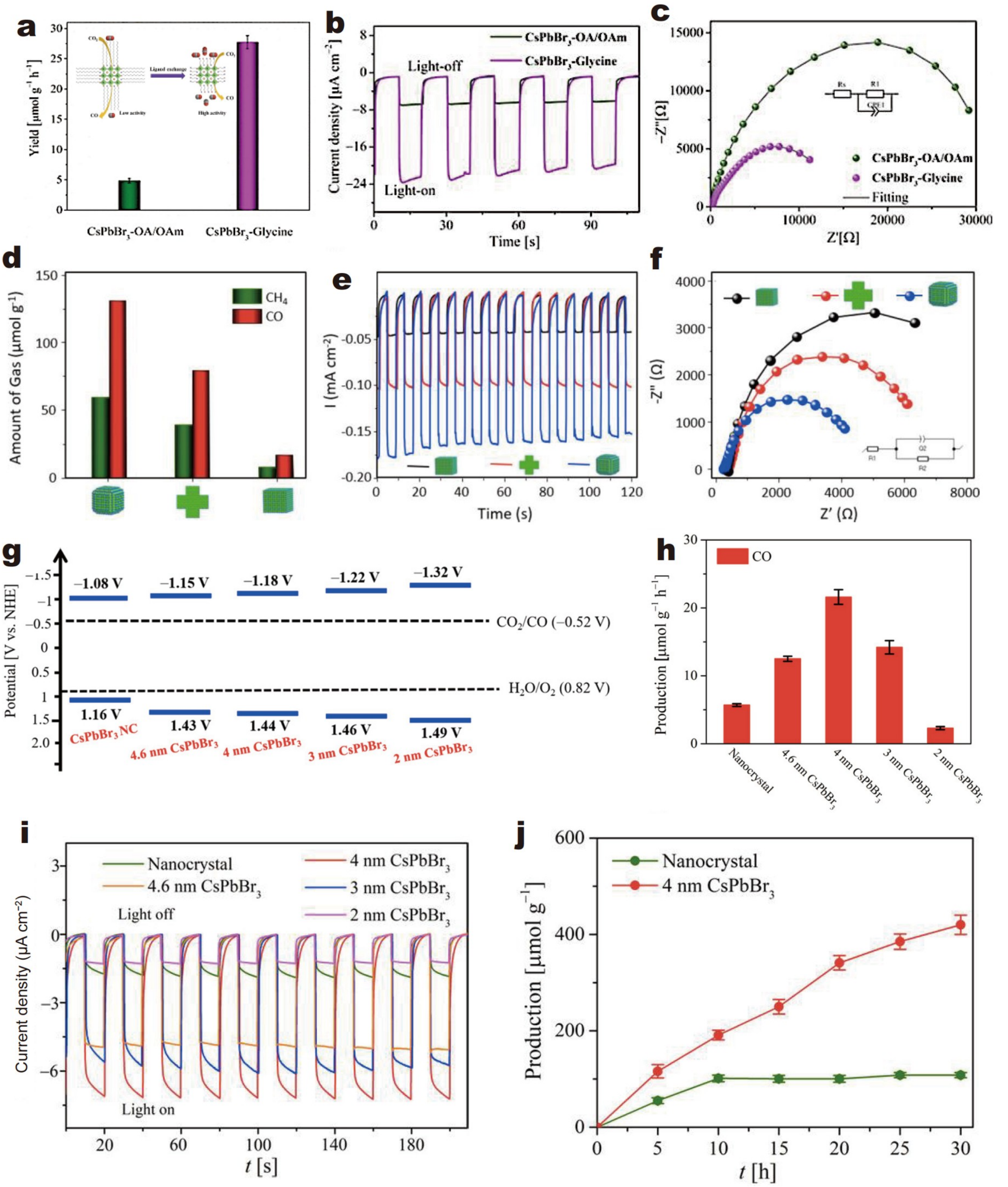

Figure 18 (a) Photocatalytic evolution of CO generated upon CO_2 reduction with $CsPbBr_3$-OA/OAm and $CsPbBr_3$-Gly NCs as the photocatalysts, and ligand exchange in $CsPbBr_3$ (inset); (b) current density-time (*I*-*t*) curves at a bias potential of −0.4 V (*vs.* Ag/AgCl); and (c) EIS Nyquist plots of $CsPbBr_3$-OA/Oam and $CsPbBr_3$-Gly. Reprinted with permission from Ref. [176], Copyright 2020, Wiley-VCH GmbH. (d) CH_4 and CO evolution during CO_2RR using multifaceted polyhedron, six-armed hexapods, and conventional six-faceted $CsPbBr_3$; (e) *I*-*t* curves and (f) EIS Nyquist plots of the multifaceted polyhedron, six-armed hexapods, and conventional six-faceted $CsPbBr_3$. Reprinted with permission from Ref. [97], Copyright 2020, American Chemical Society. (g) Schematic illustration of band structures of $CsPbBr_3$ NCs and $CsPbBr_3$ NSs; (h) the comparison of CO production with $CsPbBr_3$ NCs and $CsPbBr_3$ NSs as photocatalysts; (i) *I*-*t* curves of $CsPbBr_3$ NCs and $CsPbBr_3$ NSs measured at a bias potential of 0.4 V (*vs.* Ag/AgCl); (j) CO evolution using $CsPbBr_3$ NCs and 4 nm $CsPbBr_3$ NSs during 30 h photocatalytic CO_2 reduction. Reprinted with permission from Ref. [178], Copyright 2021, Wiley-VCH GmbH.

of active sites and boost the photocatalytic performance of $CsPbX_3$. Multifaceted polyhedron six-armed hexapods and conventional six-faceted $CsPbBr_3$ NCs demonstrated an interesting photocatalytic activity in CO_2RRs (Fig. 18d) [97]. Among these, six-faceted NCs showed the lowest catalytic activity for CO_2 reduction, with the maximum yields of CO and CH_4 being 16.4 and 7.4 μmol g^{-1}, respectively. The hexapod structure exhibited medium photocatalytic activity, while the polyhedron

$CsPbBr_3$ NCs with 26 facets indicated the strongest photocatalytic activity among the three structures, yielding 130.7 and 58.8 μmol g^{-1} of CO and CH_4, respectively. This confirmed that charge-carrier separation is more efficient in multifaceted $CsPbBr_3$ NCs than in standard six-faceted cube nanostructures. Cube-shaped nanostructures showed efficient carrier recombination with high PLQYs (>50%). However, the charge carriers in multifaceted structures were trapped and resulted in poor emission with PLQY of ~1%, demonstrating enhanced photocurrent and lower charge-carrier resistance (Fig. 18e, f) and enhanced photocatalytic performance [97].

In addition to multifaceted MHPs, 2D structures exhibited unique advantages, including increased stability in aqueous systems, abundant active sites for CO_2 reduction, and reduced bulk recombination [178]. The 2D $CsPbBr_3$ NSs possess a higher bandgap than NCus, revealing stronger driving forces that trigger the reduction of CO_2 to CO, and H_2O to O_2 (Fig. 18g). The $CsPbBr_3$ NSs with a thickness of 4 nm exhibited high photocatalytic activity in CO_2 reduction, with a CO formation rate of 21.6 μmol g^{-1} h^{-1}, which is 3.8 times higher than that of $CsPbBr_3$ NCs (5.7 μmol g^{-1} h^{-1}) (Fig. 18h) [178]. High photocurrent density further reinforces the photocatalytic performance of 4-nm $CsPbBr_3$ NSs, indicating significantly higher charge-carrier separation compared with NCs, and NSs with different thicknesses, i.e., 2, 3, and 4.6 nm $CsPbBr_3$ (Fig. 18i). The 2D $CsPbBr_3$ demonstrated excellent stability and performance for up to 30 h (Fig. 18j).

Anion substitution

Mixed halide perovskites proved to be more photoactive compared with solely $CsPbBr_3$. For example, polymerization of 2,2′,5′,2″-*ter*-3,4-ethylene-dioxythiophene (TerEDOT) over a series of mixed MHPs ($CsPbX_3$, X = I, $I_{0.67}Br_{0.33}$, $I_{0.5}Br_{0.5}$, $Br_{0.67}I_{0.33}$, Br) demonstrated higher photocatalytic activity when iodine was added in the crystal structure. It was shown that $CsPbI_3$ QDs exhibited the most efficient performance due to their narrow bandgap and low exciton binding energy, which was further confirmed with high charge-transport efficiency (Φ) [177]. A series of 2D $CsPbBr_{3-x}I_x$ (x = 0.3, 0.6, 0.9) NSs were also investigated for CO_2 reduction. Compared with $CsPbBr_3$ NSs, all the $CsPbBr_{3-x}I_x$ exhibit improved photocatalytic activity (Fig. 19a, b), due to the enhanced visible light-harvesting capacity by replacing Br^- with I^- [178]. However, an excess of iodide content can result in the lower photocatalytic performance of $CsPb_{3-x}I_x$, probably due to the decrease in the thermodynamic driving force for catalytic CO_2 photoreduction [178]. Fourfold higher amount of bromide in $CsPbBr_{2.4}I_{0.6}$ proved optimal for best photocatalytic activity and charge-carrier separation (Fig. 19c) [178]. Recently, Knezevic *et al.* [137] demonstrated photocatalytic hydrogen generation using $CsPbBr_{1.95}I_{1.05}@TiO_2$, reaching 250 μmol g^{-1} of H_2 after 3 h of irradiation. An optimal room-temperature substitution of bromide with iodide is crucial for hydrogen generation together with a thin TiO_2 overlayer, essential in both MHP stability and interfacial charge transfer.

Anion substitution strategy was also used to boost the photocatalytic performance of $CsPb(Br_xCl_{1-x})_3$ (x = 1, 0.7, 0.5, 0.3, 0) for CO_2 reduction, indicating that $CsPbBr_{0.5}Cl_{0.5}$ was the best catalyst, with a total generation rate of CO and CH_4 up to 875 μmol g^{-1}, which is almost 4.5 and 9.1 times higher than that of pristine $CsPbBr_3$ and $CsPbCl_3$, respectively (Fig. 19d) [179]. Furthermore, the selectivity toward CO and CH_4 of all $CsPb(Br_xCl_{1-x})_3$ was up to 99%, and the common H_2 byproduct was not obtained (Fig. 19e). The high yield of $CsPb(Br_xCl_{1-x})_3$ in CO_2 photoreduction was explained by the efficient charge separation and moderate stability in mixed-halide perovskites [179]. Transient photocurrent responses were also used to explain the predominant photocatalytic activity of $CsPb(Br_{0.5}Cl_{0.5})_3$, revealing slightly higher charge carrier density of $CsPb(Br_{0.5}Cl_{0.5})_3$, being essential for charge-carrier separation (Fig. 19f).

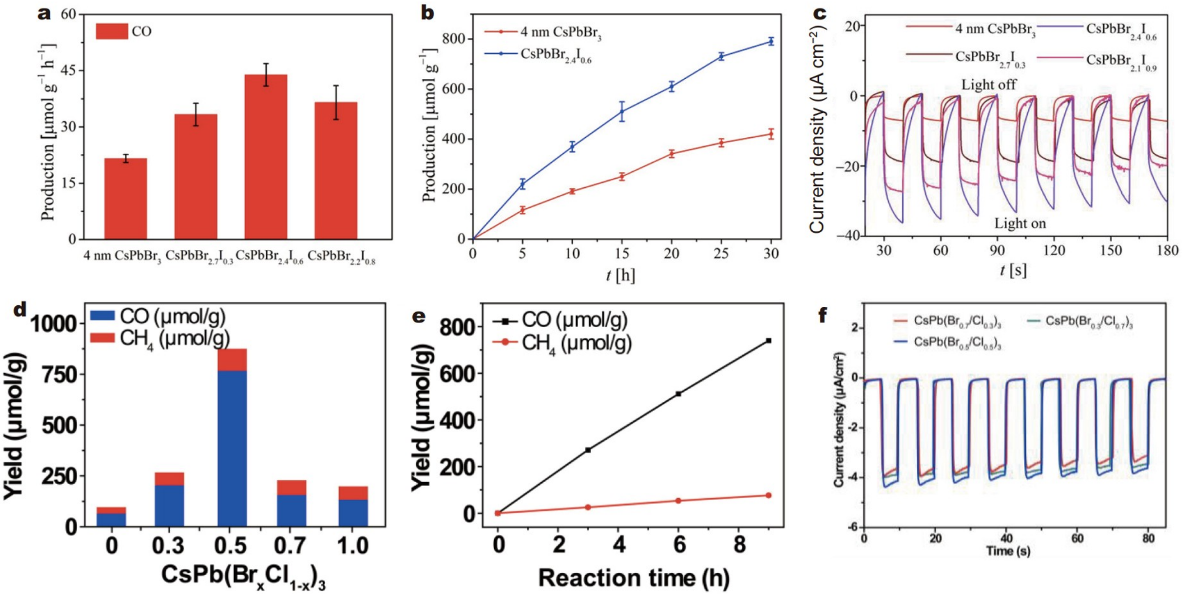

Figure 19 (a) Photocatalytic evolution of CO upon anion substitution of bromide; (b) CO evolution during 30 h photocatalytic reaction using 4 nm $CsPbBr_3$ NSs and $CsPbBr_{3-x}I_x$ NSs; (c) *I-t* curves of 4 nm $CsPbBr_3$ and $CsPbBr_{3-x}I_x$ NSs. Reprinted with permission from Ref. [178], Copyright 2021, Wiley-VCH GmbH. (d) Evolution of CO and CH_4 using $CsPb(Br_x/Cl_{1-x})_3$ (x = 1, 0.7, 0.5, 0.3, 0); (e) CO and CH_4 generation rates using $CsPb(Br_{0.5}/Cl_{0.5})_3$ as the catalyst; (f) transient photocurrent responses of mixed halide $CsPb(Br_x/Cl_{1-x})_3$ (x = 0.7, 0.5, 0.3) NCs. Reprinted with permission from Ref. [179], Copyright 2018, Elsevier Inc.

Doping with metals

Doping with metals represents a valid approach to elevate the photocatalytic performance of $CsPbX_3$. Shyamal *et al.* [180] successfully demonstrated the photocatalytic performance of 3% Fe(II)-doped $CsPbBr_3$ and its selectivity towards CH_4 instead of CO (Fig. 20a). EIS Nyquist plots show excellent charge-carrier separation in Fe-doped MHP due to the electron transfer (Fig. 20b), as well as high photocurrent response for 3% doping, i.e., 25% in crude solution (Fig. 20c). Moreover, the Fe:$CsPbBr_3$ photocatalyst does not require any additional carrier transportation material or heterostructures like other $CsPbBr_3$ systems (e.g., $CsPbBr_3$/graphene QDs, g-C_3N_4 and Pd-NSs) [180]. Besides Fe(II)-doped $CsPbBr_3$ perovskite NCs, Mn-doped CsPb(Br/Cl)$_3$ mixed-halide MHPs for CO_2 photoreduction were reported [181]. A series of CsPb(Br/Cl)$_3$:Mn perovskites, (samples: 1–4, Pb:Mn = 4:1, 2:1, 2:3, 3:7) showed good photocatalytic activities in CO_2 conversion to CO and CH_4, with 2:1 ratio demonstrating the highest yield, reaching 1917 and 82 μmol g^{-1} for CO and CH_4, respectively, being 14.2 and 1.4 times higher than those of $CsPbBr_3$. Zhang's group [182] reported improved photocatalytic performance of cobalt-doped $CsPbBr_3/Cs_4PbBr_6$ for CO_2 reduction. $CsPbBr_3/Cs_4PbBr_6$ NCs with 0.5%–3% cobalt doping were employed as photocatalysts for CO_2 reduction in pure water due to the increased stability upon coating with hexafluorobutyl methacrylate hydrophobic surface layer. $Co_{2\%}@CsPbBr_3/Cs_4PbBr_6$ heterojunction perovskite showed the highest efficiency for photocatalytic CO_2 conversion into CO and CH_4, with an impressive overall yield of 247 μmol g^{-1} under visible light irradiation (Fig. 20d). Co-doping extends the PL lifetime of photogenerated electrons, making transporting them to the acceptor in the reduction process easier. EIS and photocurrent response measurements were also used to investigate the effect of Co doping on charge-carrier transfer and separation efficiency (Fig. 20e, f) [182]. The Nyquist plot of $Co_{2\%}@CsPbBr_3/Cs_4PbBr_6$ NCs experience a much smaller semicircle diameter than pristine $CsPbBr_3/Cs_4PbBr_6$ NCs, indicating that Co doping creates more active sites and hence promotes charge transfer from NCs to other components in the reaction system.

Ding *et al.* [183] reported photocatalytic activity of Zn^{2+}-doped $CsPbBr_3$ NCs for hydrogen generation from water, with Na_2S and Na_2SO_3 used as the sacrificial agent. In Zn^{2+}-doped $CsPbBr_3$, photogenerated electrons are transferred to Zn active site, where proton reduction occurs. Zn-doped MHPs NCs outperformed pure $CsPbBr_3$ NCs in the evolution of hydrogen in water, with a hydrogen production rate of 127 μmol g^{-1} [183].

Construction of heterojunctions with perovskites

$CsPbX_3$ coupled with metal complexes that can serve as co-catalysts is also regarded as a useful strategy to enhance photocatalytic performance, i.e., Ni(tpy) (nickel complex with 2,2′:6′,2″-terpyridine, $[Ni(terpy)_2]^{2+}$) [184] and $Re(CO)_3Br$(dcbpy) [173]. Ni(tpy) can supply specific catalytic sites and serve as electron sinks to avoid electron–hole recombination in $CsPbBr_3$ NCs. As a result, the yield of CO/CH_4 increased dramatically, reaching 1724 μmol g^{-1} CO/CH_4, which is nearly 26 times higher than that of pristine $CsPbBr_3$ (Fig. 21a, e). The introduction of $Re(CO)_3Br$(dcbpy) onto $CsPbBr_3$ NCs can serve as a co-catalyst with high catalytic activity and CO selectivity (Fig. 21b, f).

Besides metal complexes, other organic molecules were used for coupling with $CsPbBr_3$ in order to enhance the photocatalytic properties through the electron transfer, e.g., methyl viologen, or ferrocene [187–189]. Furthermore, MHPs could be coupled to heterogeneous components such as poly(3-hex-

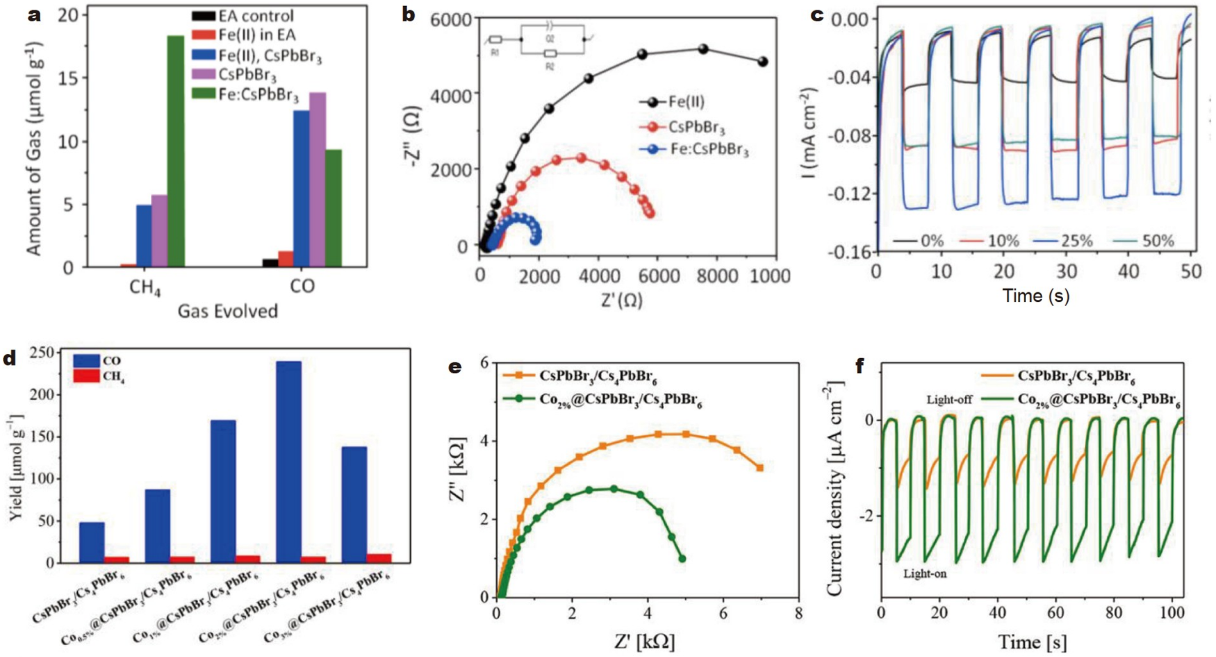

Figure 20 (a) Evolution of CH_4 and CO using Fe-doped $CsPbBr_3$; (b) EIS Nyquist plots; and (c) *I-t* curves at a bias potential of −0.4 V (*vs.* Ag/AgCl) of Fe-doped $CsPbBr_3$, where 25% represents the amount of Fe in crude solution corresponding to 3% Fe doping. Reprinted with permission from Ref. [180], Copyright 2019, American Chemical Society. (d) Yields of CO_2 reduction using variable substitution ration of $CsPb(Br_x/Cl_{1-x})_3$. (e) EIS Nyquist plots; and (f) *I-t* curves at a bias potential of −0.4 V (*vs.* Ag/AgCl) of $CsPbBr_3/Cs_4PbBr_6$ and $Co_{2\%}@CsPbBr_3/Cs_4PbBr_6$. Reprinted with permission from Ref. [182], Copyright 2019, Wiley-VCH Verlag GmbH & Co. KGaA,Weinheim.

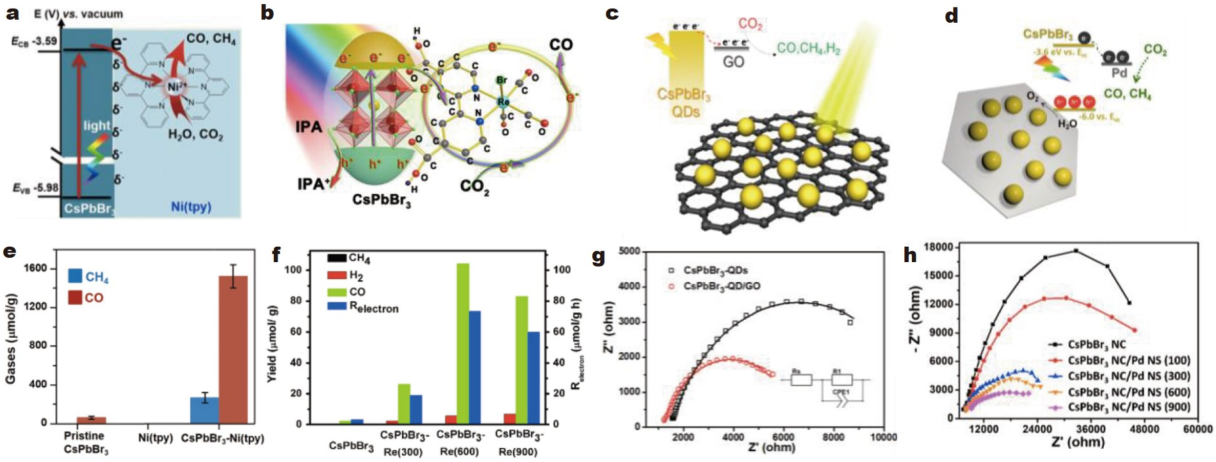

Figure 21 Schematic representation of CO_2 photoreduction over (a) $CsPbBr_3$-Ni(tpy) [184]; (b) $CsPbBr_3$- Re(CO)$_3$Br(dcbpy) [173]; (c) $CsPbBr_3$ QD/GO [185]; and (d) $CsPbBr_3$ NC/Pd NS photocatalysts [186]. The yield of CO_2 reduction products using (e) $CsPbBr_3$-Ni(tpy) [184]; and (f) $CsPbBr_3$-Re(CO)$_3$Br(dcbpy) as photocatalysts [173]. EIS Nyquist plots of (g) $CsPbBr_3$/GO [185]; (h) $CsPbBr_3$ NC/Pd NSs [186]. Reprinted with permission from Refs [173,184–186], Copyright 2020, American chemical Society, 2019 WILEY-VCH Verlag GmbH & Co. KGaA, Weinheim, Copyright 2017, American chemical Society, and Copyright 2018, American chemical Society, respectively.

ylthiophene-2,5-diyl) (P3HT) polymer [189], fullerene [190], MXene NSs [191], and porous g-C_3N_4 (PCN) [192], in order to promote interfacial charge transfer. In such a configuration, MHPs provide better photocatalytic activity than the pristine $CsPbBr_3$, with a good to excellent yield of products, due to the charge separation that determines the yield of the whole process.

For example, in the CO_2RR using solely $CsPbBr_3$ as a photocatalyst, the amounts of CO and CH_4 formed after 12 h were 49.5 and 22.9 μmol g^{-1}. After the introduction of GO, the obtained yield slightly increased to 58.8 and 29.6 μmol g^{-1} for CO and CH_4, respectively (Fig. 21c) [185]. Although the CO and CH_4 generation rate is quite low, GO facilitates charge-carrier separation *via* electron transfer, as evidenced by the Nyquist results (Fig. 21g, h). However, one must consider the possible carbon oxidation that could lead to the apparent CO and CO_2 yield increase [193]. In order to reinforce GO influence, bandgap modification through anion exchange could be a possible solution. The charge separation efficiency could also be improved by loading $CsPbBr_3$ NCs on graphitic carbon nitride containing titanium-oxide species (TiO–CN) [194]. The introduction of TiO–CN led to the swift interfacial charge separation between $CsPbBr_3$ and TiO–CN due to their favorable energy offset and strong chemical bonding, which enhanced the photocatalytic activity of $CsPbBr_3$@TiO–CN in the CO_2 reduction to CO. Particularly, the rate of CO formation when using $CsPbBr_3$@TiO–CN as the photocatalyst was 129 μmol g^{-1}, which was over 3 times and 6 times higher than those of pristine $CsPbBr_3$ and TiO–CN, respectively. Interestingly, Pd NSs can act as an electron acceptor and co-catalyst in CO_2 reduction [186]. As a result, the introduction of Pd NSs boosts the photocatalytic performance of $CsPbBr_3$, with a CO generation rate of 12.633 μmol g^{-1}, which is a 2.4-fold increase compared with the pristine $CsPbBr_3$ (Fig. 21d, h).

Encapsulation of perovskites

As previously mentioned, $CsPbX_3$ NCs are unstable in polar reaction systems, and their catalytic activity is reduced. To meet this challenge, encapsulation is considered as an efficient strategy to protect the $CsPbBr_3$ surface as well as to promote their photocatalytic performance. Up to date, several studies have been carried out, including coating with a thin graphdiyne (GDY) layer [195], silica, TiO_2, and polymers such as polymer-polyaniline (PANI). Under the protection of GDY, the stability of $CsPbBr_3$ in an aqueous photocatalytic system was improved. Moreover, the surface was decorated with Co, and thus the CO formation rate was also increased, reaching 10.2 μmol g^{-1}, which was 3.1 times higher than that of pure $CsPbBr_3$ (Fig. 22a). Low charge-transfer resistance was observed for samples containing GDY, demonstrating successful interfacial charge transfer (Fig. 22b) and stability for over 36 h long photocatalytic reaction (Fig. 22c). The silica encapsulation demonstrated the effective removal of methyl orange under visible light. Moreover, $CsPbBr_3/SiO_2$ proved to be efficient for generating singlet oxygen through energy transfer [196].

To improve the stability of $CsPbBr_3$ NCs in photocatalytic water splitting reaction, Zou's group [174] used conductive PANI as the encapsulating material for the NCs. The PANI-coated $CsPbBr_3$ NCs could remain stable for approximately 11 days, while pure $CsPbBr_3$ decomposed into a white precipitate very quickly. The $CsPbBr_3$@PANI was then used for the hydrogen generation, achieving high photocatalytic performance, with the H_2 formation yield of 4.81 mmol h^{-1} g^{-1} and the stability in 120 h [174].

A chemically stable amorphous TiO_2 (a-TiO_2) has been identified as both an excellent protective layer (Fig. 22d) and an electron transfer layer (Fig. 22e). The photocatalytic performance of $CsPbBr_3$ NC and $CsPbBr_3$ NC/a-TiO_2 (anatase crystalline form) was investigated in CO_2RR, and the results showed that the yield of reaction products (CO and CH_4) increased significantly after the encapsulation with a-TiO_2 (Fig. 22f) [132]. The improvement in photocatalytic performances comes from the band position of a-TiO_2, which can build band energy offset with $CsPbBr_3$ NC and provide an additional deactivation pathway through electron transfer (Fig. 22e) [132]. The *in situ* growth of halide perovskites ($Cs_3Bi_2Br_9$ and $Cs_2AgBiBr_6$) in a mesoporous titania framework showed enhancement of the

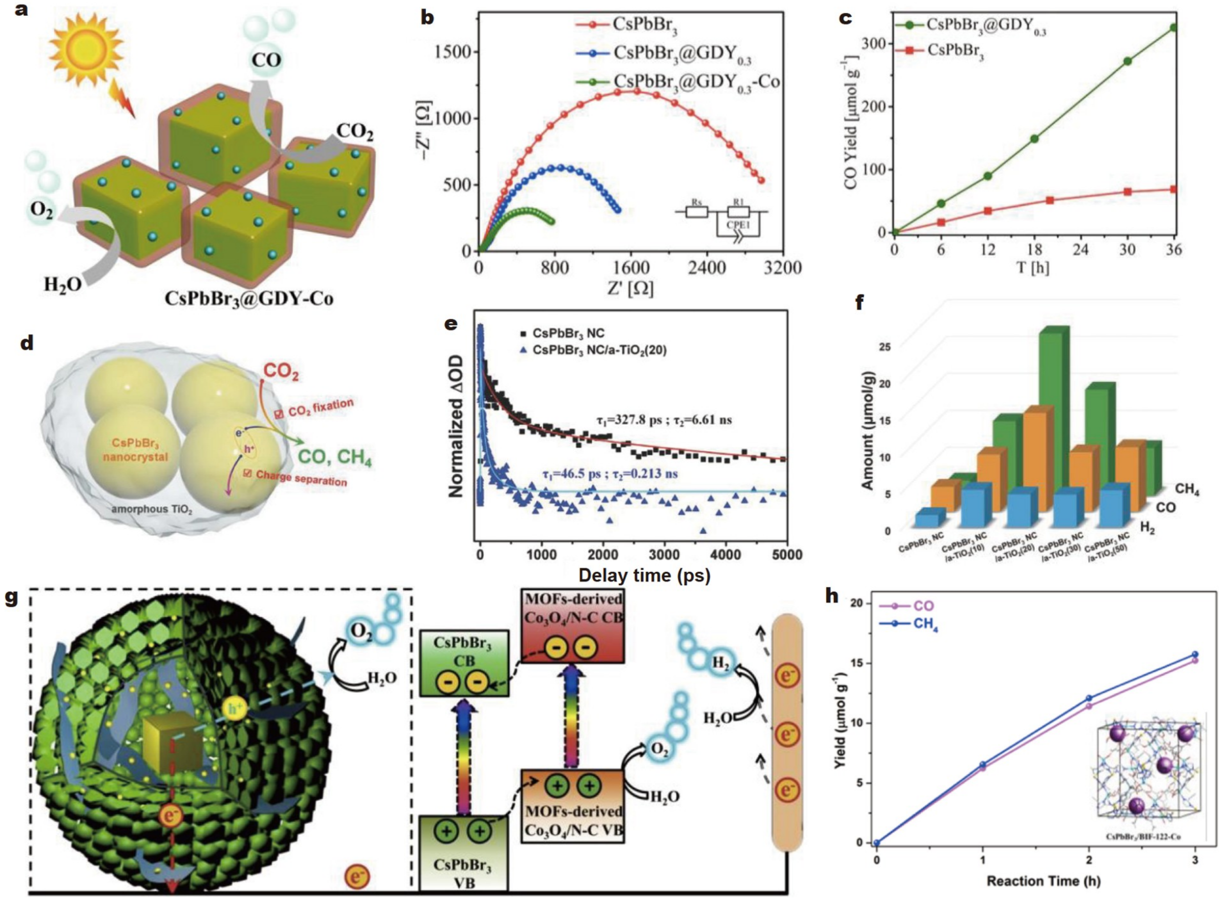

Figure 22 (a) Schematic illustration of the photocatalytic reaction over $CsPbBr_3$@GDY-Co; (b) EIS Nyquist plots of $CsPbBr_3$@GDY-Co; (c) photocatalytic evolution using $CsPbBr_3$@GDY-Co. Reprinted with permission from Ref. [195], Copyright 2020, American Chemical Society. (d) Schematic illustration of the enhanced charge separation and CO_2 fixation in a-TiO_2-encapsulated $CsPbBr_3$ NC; (e) TAS decay curves demonstrating electron transfer from MHP to TiO_2; (f) evolution of CH_4, CO, and H_2 using a-TiO_2-encapsulated $CsPbBr_3$ as photocatalysts. Reprinted with permission from Ref. [132], 2018 WILEY-VCH Verlag GmbH & Co. KGaA, Weinheim. (g) Illustration of the chemical immobilization effect induced by MOFs-derived Co_3O_4/N-doped C framework to enhance the aqueous stability of CPB NC. Reprinted with permission from Ref. [199], Copyright 2019, Published by Elsevier B.V. (h) CH_4 and CO evolution using encapsulated $CsPbBr_3$ by BIF-122-Co and its schematic representation. Reprinted with permission from Ref. [200], Copyright 2021, American Chemical Society.

CO_2RR [197]. The built-in electric field at the interface of the perovskite nanodots and titania channels promoted the photogenerated charge transfer, leading to higher selectivity toward CH_4 generation. In other work, ultrathin and small-size GO (USGO) NSs were employed as the electron mediator to construct an efficient Z-scheme system by combining $CsPbBr_3$ with α-Fe_2O_3. The heterojunction demonstrated improved efficiency for visible-light-driven CO_2RR with water as the electron source [198].

Metal-organic frameworks (MOFs), such as ZIF-67-derived Co_3O_4 and MIL-88-derived FeO_x, have proved to be efficient photoanode materials for photoelectrochemical water oxidation [199]. Yin's group [199] demonstrated $CsPbBr_3$@MOFs-derived Co_3O_4/N-doped carbon core/shell composite (MHP@Co_3O_4/N–C). The unique N–Br halogen bonds are formed between pyrrodic-N from N-frameworks and the Br atom from $CsPbBr_3$ NCs. Due to this distinct chemical bonding immobilization effect introduced by the MOFs-derived Co_3O_4/N–C frameworks, the decomposition of $CsPbBr_3$ in an aqueous solution can be effectively inhibited, thus greatly enhancing the stability of MHP@Co_3O_4/N–C system (Fig. 22g). Such a configuration results in the unique type-II heterojunction, allowing charge-carrier separation, where holes are accumulated into the VB of the MOF and electrons are flowing to the CB of MHP, enhancing the photocatalytic performance of pristine MHP, while acting as a co-catalyst during water oxidation.

Boron imidazolate frameworks (BIFs) have recently attracted a lot of interest in the field of CO_2 reduction [200]. Due to the electron-deficient property of B and the presence of active B–H sites in the internal pore surface, the affinity of BIF with the confined perovskite could be directly increased, and thus provide an interfacial contact [200]. The terminal oxygen in BIFs can coordinate with Pb^{2+} cations, which induces preferential nucleation of $CsPbX_3$ crystals. Therefore, BIFs could be suitable for perovskite encapsulation and catalytic activity improvement toward CO_2RR. Chen *et al.* [200] designed and synthesized ctn-type microporous BIF (cation) $[Co_3[BH(2\text{-ipim})_3]_2(BTC)_2]_n$ (BIF-122-Co; with ipim = isopropylimidazolate and BTC = 1,3,5-benzenetricarboxylate) and used it as a host matrix to encapsulate $CsPbBr_3$, to afford a perovskite-BIF composite, $CsPbBr_3$/BIF-122-Co. The porous skeleton of BIF-122-Co in the composite material could considerably improve the stability of the $CsPbBr_3$ perovskite in the photocatalytic reaction system (Fig. 22h, inset). The photocatalytic activity of $CsPbBr_3$/BIF-122-Co in H_2O/ethyl acetate exhibits high activity in CO_2RR with the total CO and CH_4 formation rates being 15.23 and 15.76 μmol g^{-1} after 3 h, respectively (Fig. 22h).

Herein, we described different strategies to enhance metal-halide perovskites' photocatalytic performance. The above-mentioned modifications have shown improved photocatalytic activity compared with the pristine $CsPbX_3$. MHP encapsulation is widely used to improve MHPs' stability and boost charge-carrier separation. However, studies have shown that surface treatment, morphology manipulation, and metal doping could highly influence both MHP stability and photocatalytic activity. One should note that coating with carbon-based materials could influence the photocatalytic yield of CO and CO_2, due to carbon oxidation [193].

CONCLUSION AND PERSPECTIVES

Metal-halide perovskites are perfect candidates for photocatalytic applications due to their optical and electronic properties. This review highlights a variety of synthetic procedures focused on the surface, morphological, and structural modifications that influence MHP's stability, optical properties, charge-carrier dynamics, and especially photocatalytic activity. We provide an overview of MHP's charge-carrier dynamics to discern charge-carrier intraband relaxation, trapping, and non-radiative and radiative recombination while considering quantum confinement, cation and anion type, metallic doping, coupling, and encapsulation of MHPs in stable materials. We then summarize the charge transfer mechanisms upon MHP coupling, encapsulation, and doping that are necessary to maximize charge-carrier separation for photocatalytic applications.

Photocatalysis requires slow charge carrier relaxation at early delay times, whereas non-radiative losses (e.g., Auger recombination) need to be minimized. At the pico- and nano-scale, the charge-carrier lifetime could be prolonged through charge transfer, resulting in PL quenching. MHPs exhibit unbalanced charge-carrier diffusion, demonstrating significantly higher diffusion of holes; this property could significantly improve oxidation reactions.

The stability and the toxicity remain, without a doubt, the major issue to overcome. While studies are discussing the protection of MHPs and claiming improved stability toward various reactions, a lack of post-reaction characterization can be observed, and the development of *in situ* characterization techniques during the photocatalytic process is needed. Moreover, new synthetic strategies should be explored to encapsulate and protect MHPs using a water-repellant organic and inorganic shell to maintain their stability in an aqueous solvent.

The versatility of the optical and electronic properties of MHPs allows the adjustment of their CB and VB potential energy for selective oxidation and reduction reactions. Simultaneous and rigorous characterization of the optical and electronic properties of modified MHPs could lead to a better correlation between the photochemical and electronic properties. The presence of defects in MHPs has not yet been explored in terms of photocatalytic reaction. The defect nature (shallow or deep) is known to affect the carrier separation, and, thus the quantum efficiency during the photocatalytic reaction. The defect nature control would enlighten a strategy to reach an effective charge carrier lifetime and better understanding of the photocatalytic reaction mechanism.

To go further, the future studies should focus on the charge-carrier dynamics and photocatalytic properties of 2D materials, i.e., NPLs and NSs. 2D cesium-lead halide-based materials could demonstrate significantly improved photocatalytic activity, due to their higher surface availability and reduced thickness that allows efficient transport of the free charge carriers to the surface of the photocatalyst.

Finally, MHP commercialization in the photocatalytic field could be attainable with the development of automated high-yield synthetic procedures and, most importantly, with stability improvements that are needed for achieving high photocatalytic activity and reproducibility. So far, the concept of MHPs' employment in photocatalysis has been demonstrated on a small scale, and medium or industrial scale is yet to be explored and developed.

Received 2 February 2023; accepted 31 March 2023;

1 Wells HL. Über die Cäsium- und kalium-bleihalogenide. Z Anorg Chem, 1893, 3: 195–210

2 Møller CK. The structure of cæsium plumbo iodide $CsPbI_3$. Mat Fys Medd Dan Vid Selsk, 1959, 32: 1–18

3 Møller CK. The structure of perovskite-like caesium plumbo trihalides. Mat Fys Medd Dan Vid Selsk, 1959, 32: 1–27

4 Møller CK. Crystal structure and photoconductivity of cæsium plumbohalides. Nature, 1958, 182: 1436

5 Rose G. Ueber einige neue mineralien des urals. J Prakt Chem, 1840, 19: 459–468

6 Goldschmidt VM. Die gesetze der krystallochemie. Naturwissenschaften, 1926, 14: 477–485

7 Cape JA, White RL, Feigelson RS. EPR study of the structure of $CsPbCl_3$. J Appl Phys, 1969, 40: 5001–5005

8 Saidaminov MI, Almutlaq J, Sarmah S, *et al.* Pure Cs_4PbBr_6: Highly luminescent zero-dimensional perovskite solids. ACS Energy Lett, 2016, 1: 840–845

9 Wang L, Liu H, Zhang Y, *et al.* Photoluminescence origin of zero-dimensional Cs_4PbBr_6 perovskite. ACS Energy Lett, 2020, 5: 87–99

10 Zhu H, Fu Y, Meng F, *et al.* Lead halide perovskite nanowire lasers with low lasing thresholds and high quality factors. Nat Mater, 2015, 14: 636–642

11 Zhang Z, Liu Y, Geng C, *et al.* Rapid synthesis of quantum-confined $CsPbBr_3$ perovskite nanowires using a microfluidic reactor. Nanoscale, 2019, 11: 18790–18796

12 Breternitz J, Schorr S. What defines a perovskite? Adv Energy Mater, 2018, 8: 1802366

13 Akkerman QA, Manna L. What defines a halide perovskite? ACS Energy Lett, 2020, 5: 604–610

14 Li Z, Yang M, Park JS, *et al.* Stabilizing perovskite structures by tuning tolerance factor: Formation of formamidinium and cesium lead iodide solid-state alloys. Chem Mater, 2016, 28: 284–292

15 Tsui KY, Onishi N, Berger RF. Tolerance factors revisited: Geometrically designing the ideal environment for perovskite dopants. J Phys Chem C, 2016, 120: 23293–23298

16 Nitsch K, Dušek M, Nikl M, *et al.* Ternary alkali lead chlorides: Crystal growth, crystal structure, absorption and emission properties. Prog Cryst Growth Charact Mater, 1995, 30: 1–22

17 Rodová M, Brožek J, Knížek K, *et al.* Phase transitions in ternary caesium lead bromide. J Thermal Anal Calorimetry, 2003, 71: 667–673

18 Marronnier A, Roma G, Boyer-Richard S, *et al.* Anharmonicity and disorder in the black phases of $CsPbI_3$ used for stable inorganic perovskite solar cells. In: Procedings of 2018 IEEE 7th World Conference on Photovoltaic Energy Conversion (WCPEC) (A Joint Conference of 45th IEEE PVSC, 28th PVSEC & 34th EU PVSEC). Waikoloa, HI: IEEE, 2018. 1715–1717

19 Protesescu L, Yakunin S, Bodnarchuk MI, *et al.* Nanocrystals of cesium lead halide perovskites ($CsPbX_3$, X = Cl, Br, and I): Novel optoelectronic materials showing bright emission with wide color gamut. Nano Lett, 2015, 15: 3692–3696
20 Heidrich K, Künzel H, Treusch J. Optical properties and electronic structure of $CsPbCl_3$ and $CsPbBr_3$. Solid State Commun, 1978, 25: 887–889
21 Ito H, Onuki H, Onaka R. Optical and photoelectronic studies of $CsPbCl_3$ and $CsPbBr_3$. J Phys Soc Jpn, 1978, 45: 2043–2044
22 Nitsch K, Hamplová V, Nikl M, *et al.* Lead bromide and ternary alkali lead bromide single crystals—Growth and emission properties. Chem Phys Lett, 1996, 258: 518–522
23 Nikl M, Nitsch K, Polák K, *et al.* Quantum size effect in the excitonic luminescence of $CsPbX_3$-like quantum dots in CsX (X = Cl, Br) single crystal host. J Lumin, 1997, 72-74: 377–379
24 Kondo S, Kakuchi M, Masaki A, *et al.* Strongly enhanced free-exciton luminescence in microcrystalline $CsPbBr_3$ films. J Phys Soc Jpn, 2003, 72: 1789–1791
25 Stoumpos CC, Malliakas CD, Peters JA, *et al.* Crystal growth of the perovskite semiconductor $CsPbBr_3$: A new material for high-energy radiation detection. Cryst Growth Des, 2013, 13: 2722–2727
26 Elbaz GA, Straus DB, Semonin OE, *et al.* Unbalanced hole and electron diffusion in lead bromide perovskites. Nano Lett, 2017, 17: 1727–1732
27 Dong Y, Gu Y, Zou Y, *et al.* Improving all-inorganic perovskite photodetectors by preferred orientation and plasmonic effect. Small, 2016, 12: 5622–5632
28 Herz LM. Charge-carrier mobilities in metal halide perovskites: Fundamental mechanisms and limits. ACS Energy Lett, 2017, 2: 1539–1548
29 Kulbak M, Cahen D, Hodes G. How important is the organic part of lead halide perovskite photovoltaic cells? Efficient $CsPbBr_3$ cells. J Phys Chem Lett, 2015, 6: 2452–2456
30 Kojima A, Teshima K, Shirai Y, *et al.* Organometal halide perovskites as visible-light sensitizers for photovoltaic cells. J Am Chem Soc, 2009, 131: 6050–6051
31 Im JH, Lee CR, Lee JW, *et al.* 6.5% efficient perovskite quantum-dot-sensitized solar cell. Nanoscale, 2011, 3: 4088–4093
32 Kim HS, Lee CR, Im JH, *et al.* Lead iodide perovskite sensitized all-solid-state submicron thin film mesoscopic solar cell with efficiency exceeding 9%. Sci Rep, 2012, 2: 591
33 Lee MM, Teuscher J, Miyasaka T, *et al.* Efficient hybrid solar cells based on meso-superstructured organometal halide perovskites. Science, 2012, 338: 643–647
34 Swarnkar A, Ravi VK, Nag A. Beyond colloidal cesium lead halide perovskite nanocrystals: Analogous metal halides and doping. ACS Energy Lett, 2017, 2: 1089–1098
35 Marronnier A, Roma G, Boyer-Richard S, *et al.* Anharmonicity and disorder in the black phases of cesium lead iodide used for stable inorganic perovskite solar cells. ACS Nano, 2018, 12: 3477–3486
36 https://www.nrel.gov/pv/cell-efficiency.html https://www.nrel.gov/pv/cell-efficiency.html
37 Huang CY, Zou C, Mao C, *et al.* $CsPbBr_3$ perovskite quantum dot vertical cavity lasers with low threshold and high stability. ACS Photonics, 2017, 4: 2281–2289
38 Jung DH, Park JH, Lee HE, *et al.* Flash-induced ultrafast recrystallization of perovskite for flexible light-emitting diodes. Nano Energy, 2019, 61: 236–244
39 Nedelcu G, Protesescu L, Yakunin S, *et al.* Fast anion-exchange in highly luminescent nanocrystals of cesium lead halide perovskites ($CsPbX_3$, X = Cl, Br, I). Nano Lett, 2015, 15: 5635–5640
40 Wang D, Li W, Du Z, *et al.* $CoBr_2$-doping-induced efficiency improvement of $CsPbBr_3$ planar perovskite solar cells. J Mater Chem C, 2020, 8: 1649–1655
41 Shapiro A, Heindl MW, Horani F, *et al.* Significance of Ni doping in $CsPbX_3$ nanocrystals *via* postsynthesis cation-anion coexchange. J Phys Chem C, 2019, 123: 24979–24987
42 Yong ZJ, Guo SQ, Ma JP, *et al.* Doping-enhanced short-range order of perovskite nanocrystals for near-unity violet luminescence quantum yield. J Am Chem Soc, 2018, 140: 9942–9951
43 Huang D, Bo J, Zheng R, *et al.* Luminescence and stability enhancement of $CsPbBr_3$ perovskite quantum dots through surface sacrificial coating. Adv Opt Mater, 2021, 9: 2100474
44 Kim H, Bae SR, Lee TH, *et al.* Enhanced optical properties and stability of $CsPbBr_3$ nanocrystals through nickel doping. Adv Funct Mater, 2021, 31: 2102770
45 Yao JS, Ge J, Han BN, *et al.* Ce^{3+}-doping to modulate photoluminescence kinetics for efficient $CsPbBr_3$ nanocrystals based light-emitting diodes. J Am Chem Soc, 2018, 140: 3626–3634
46 Yin J, Ahmed GH, Bakr OM, *et al.* Unlocking the effect of trivalent metal doping in all-inorganic $CsPbBr_3$ perovskite. ACS Energy Lett, 2019, 4: 789–795
47 Lozhkina OA, Murashkina AA, Shilovskikh VV, *et al.* Invalidity of band-gap engineering concept for Bi^{3+} heterovalent doping in $CsPbBr_3$ halide perovskite. J Phys Chem Lett, 2018, 9: 5408–5411
48 Tong Y, Bladt E, Aygüler MF, *et al.* Highly luminescent cesium lead halide perovskite nanocrystals with tunable composition and thickness by ultrasonication. Angew Chem Int Ed, 2016, 55: 13887–13892
49 Hoffman JB, Schleper AL, Kamat PV. Transformation of sintered $CsPbBr_3$ nanocrystals to cubic $CsPbI_3$ and gradient $CsPbBr_xI_{3-x}$ through halide exchange. J Am Chem Soc, 2016, 138: 8603–8611
50 Su Y, Chen X, Ji W, *et al.* Highly controllable and efficient synthesis of mixed-halide $CsPbX_3$ (X = Cl, Br, I) perovskite QDs toward the tunability of entire visible light. ACS Appl Mater Interfaces, 2017, 9: 33020–33028
51 Mandal S, Roy D, De CK, *et al.* Instantaneous, room-temperature, open-air atmosphere, solution-phase synthesis of perovskite quantum dots through halide exchange employing non-metal based inexpensive HCl/HI: Ensemble and single particle spectroscopy. Nanoscale Adv, 2019, 1: 3506–3513
52 van der Stam W, Geuchies JJ, Altantzis T, *et al.* Highly emissive divalent-ion-doped colloidal $CsPb_{1-x}M_xBr_3$ perovskite nanocrystals through cation exchange. J Am Chem Soc, 2017, 139: 4087–4097
53 Thawarkar S, Rana PJS, Narayan R, *et al.* Ni-doped $CsPbBr_3$ perovskite: Synthesis of highly stable nanocubes. Langmuir, 2019, 35: 17150–17155
54 Bi C, Wang S, Li Q, *et al.* Thermally stable copper(II)-doped cesium lead halide perovskite quantum dots with strong blue emission. J Phys Chem Lett, 2019, 10: 943–952
55 Wang B, Liu L, Liu B, *et al.* Study on fluorescence properties and stability of Cu^{2+}-substituted $CsPbBr_3$ perovskite quantum dots. Physica B-Condensed Matter, 2020, 599: 412488
56 Pan Q, Hu H, Zou Y, *et al.* Microwave-assisted synthesis of high-quality “all-inorganic” $CsPbX_3$ (X = Cl, Br, I) perovskite nanocrystals and their application in light emitting diodes. J Mater Chem C, 2017, 5: 10947–10954
57 Li Y, Huang H, Xiong Y, *et al.* Revealing the formation mechanism of $CsPbBr_3$ perovskite nanocrystals produced *via* a slowed-down microwave-assisted synthesis. Angew Chem Int Ed, 2018, 57: 5833–5837
58 Liu W, Zheng J, Cao S, *et al.* General strategy for rapid production of low-dimensional all-inorganic $CsPbBr_3$ perovskite nanocrystals with controlled dimensionalities and sizes. Inorg Chem, 2018, 57: 1598–1603
59 Liu H, Wu Z, Gao H, *et al.* One-step preparation of cesium lead halide $CsPbX_3$ (X = Cl, Br, and I) perovskite nanocrystals by microwave irradiation. ACS Appl Mater Interfaces, 2017, 9: 42919–42927
60 Long Z, Ren H, Sun J, *et al.* High-throughput and tunable synthesis of colloidal $CsPbX_3$ perovskite nanocrystals in a heterogeneous system by microwave irradiation. Chem Commun, 2017, 53: 9914–9917
61 Rao L, Tang Y, Song C, *et al.* Polar-solvent-free synthesis of highly photoluminescent and stable $CsPbBr_3$ nanocrystals with controlled shape and size by ultrasonication. Chem Mater, 2019, 31: 365–375
62 Tong Y, Yao EP, Manzi A, *et al.* Spontaneous self-assembly of perovskite nanocrystals into electronically coupled supercrystals: Toward filling the green gap. Adv Mater, 2018, 30: 1801117
63 Duong T, Mulmudi HK, Shen H, *et al.* Structural engineering using rubidium iodide as a dopant under excess lead iodide conditions for high efficiency and stable perovskites. Nano Energy, 2016, 30: 330–340

64 Zhai W, Lin J, Li Q, *et al.* Solvothermal synthesis of ultrathin cesium lead halide perovskite nanoplatelets with tunable lateral sizes and their reversible transformation into Cs_4PbBr_6 nanocrystals. Chem Mater, 2018, 30: 3714–3721
65 Zhai W, Lin J, Li C, *et al.* Solvothermal synthesis of cesium lead halide perovskite nanowires with ultra-high aspect ratios for high-performance photodetectors. Nanoscale, 2018, 10: 21451–21458
66 Chen M, Zou Y, Wu L, *et al.* Solvothermal synthesis of high-quality all-inorganic cesium lead halide perovskite nanocrystals: From nanocube to ultrathin nanowire. Adv Funct Mater, 2017, 27: 1701121
67 Chen D, Chen X, Li J, *et al.* Ultrathin $CsPbX_3$ (X = Cl, Br, I) nanoplatelets: Solvothermal synthesis and optical spectroscopic properties. Dalton Trans, 2018, 47: 9845–9849
68 Li ZJ, Hofman E, Davis AH, *et al.* General strategy for the growth of $CsPbX_3$ (X = Cl, Br, I) perovskite nanosheets from the assembly of nanorods. Chem Mater, 2018, 30: 3854–3860
69 Chen M, Hu H, Tan Y, *et al.* Controlled growth of dodecapod-branched $CsPbBr_3$ nanocrystals and their application in white light emitting diodes. Nano Energy, 2018, 53: 559–566
70 Li X, Wu Y, Zhang S, *et al.* $CsPbX_3$ quantum dots for lighting and displays: Room-temperature synthesis, photoluminescence superiorities, underlying origins and white light-emitting diodes. Adv Funct Mater, 2016, 26: 2435–2445
71 Wei S, Yang Y, Kang X, *et al.* Room-temperature and gram-scale synthesis of $CsPbX_3$ (X = Cl, Br, I) perovskite nanocrystals with 50–85% photoluminescence quantum yields. Chem Commun, 2016, 52: 7265–7268
72 Akkerman QA, Park S, Radicchi E, *et al.* Nearly monodisperse insulator Cs_4PbX_6 (X = Cl, Br, I) nanocrystals, their mixed halide compositions, and their transformation into $CsPbX_3$ nanocrystals. Nano Lett, 2017, 17: 1924–1930
73 Palazon F, Urso C, De Trizio L, *et al.* Postsynthesis transformation of insulating Cs_4PbBr_6 nanocrystals into bright perovskite $CsPbBr_3$ through physical and chemical extraction of CsBr. ACS Energy Lett, 2017, 2: 2445–2448
74 Wu L, Hu H, Xu Y, *et al.* From nonluminescent Cs_4PbX_6 (X = Cl, Br, I) nanocrystals to highly luminescent $CsPbX_3$ nanocrystals: Water-triggered transformation through a CsX-stripping mechanism. Nano Lett, 2017, 17: 5799–5804
75 Yang L, Wang T, Min Q, *et al.* High water resistance of monoclinic $CsPbBr_3$ nanocrystals derived from zero-dimensional cesium lead halide perovskites. ACS Omega, 2019, 4: 6084–6091
76 Zhu ZY, Yang QQ, Gao LF, *et al.* Solvent-free mechanosynthesis of composition-tunable cesium lead halide perovskite quantum dots. J Phys Chem Lett, 2017, 8: 1610–1614
77 Liu X, Gao J, Zhou G, *et al.* Low molecular weight molecule induces the effective stabilization of $CsPbBr_3$ in water. J Mol Liquids, 2020, 299: 112199
78 Wang B, Zhang C, Zheng W, *et al.* Large-scale synthesis of highly luminescent perovskite nanocrystals by template-assisted solid-state reaction at 800°C. Chem Mater, 2020, 32: 308–314
79 Pan A, He B, Fan X, *et al.* Insight into the ligand-mediated synthesis of colloidal $CsPbBr_3$ perovskite nanocrystals: The role of organic acid, base, and cesium precursors. ACS Nano, 2016, 10: 7943–7954
80 Lu C, Wright MW, Ma X, *et al.* Cesium oleate precursor preparation for lead halide perovskite nanocrystal synthesis: The influence of excess oleic acid on achieving solubility, conversion, and reproducibility. Chem Mater, 2019, 31: 62–67
81 Zhang Y, Siegler TD, Thomas CJ, *et al.* A "tips and tricks" practical guide to the synthesis of metal halide perovskite nanocrystals. Chem Mater, 2020, 32: 5410–5423
82 Li M, Zhang X, Du Y, *et al.* Colloidal $CsPbX_3$ (X = Br, I, Cl) NCs: Morphology controlling, composition evolution, and photoluminescence shift. J Lumin, 2017, 190: 397–402
83 Liang Z, Zhao S, Xu Z, *et al.* Shape-controlled synthesis of all-inorganic $CsPbBr_3$ perovskite nanocrystals with bright blue emission. ACS Appl Mater Interfaces, 2016, 8: 28824–28830
84 Balakrishnan SK, Kamat PV. Ligand assisted transformation of cubic $CsPbBr_3$ nanocrystals into two-dimensional $CsPb_2Br_5$ nanosheets. Chem Mater, 2018, 30: 74–78
85 Xiao M, Hao M, Lyu M, *et al.* Surface ligands stabilized lead halide perovskite quantum dot photocatalyst for visible light-driven hydrogen generation. Adv Funct Mater, 2019, 29: 1905683
86 Akkerman QA, Motti SG, Srimath Kandada AR, *et al.* Solution synthesis approach to colloidal cesium lead halide perovskite nanoplatelets with monolayer-level thickness control. J Am Chem Soc, 2016, 138: 1010–1016
87 Ye F, Zhang H, Li W, *et al.* Ligand-exchange of low-temperature synthesized $CsPbBr_3$ perovskite toward high-efficiency light-emitting diodes. Small Methods, 2019, 3: 1800489
88 Li J, Xu L, Wang T, *et al.* 50-fold EQE improvement up to 6.27% of solution-processed all-inorganic perovskite $CsPbBr_3$ QLEDs *via* surface ligand density control. Adv Mater, 2017, 29: 1603885
89 De Roo J, Ibáñez M, Geiregat P, *et al.* Highly dynamic ligand binding and light absorption coefficient of cesium lead bromide perovskite nanocrystals. ACS Nano, 2016, 10: 2071–2081
90 Zhang D, Eaton SW, Yu Y, *et al.* Solution-phase synthesis of cesium lead halide perovskite nanowires. J Am Chem Soc, 2015, 137: 9230–9233
91 Tang X, Han S, Zu Z, *et al.* All-inorganic perovskite $CsPb_2Br_5$ microsheets for photodetector application. Front Phys, 2018, 5: 69
92 Jing Q, Xu Y, Su Y, *et al.* A systematic study of the synthesis of cesium lead halide nanocrystals: Does Cs_4PbBr_6 or $CsPbBr_3$ form? Nanoscale, 2019, 11: 1784–1789
93 Zhang Y, Saidaminov MI, Dursun I, *et al.* Zero-dimensional Cs_4PbBr_6 perovskite nanocrystals. J Phys Chem Lett, 2017, 8: 961–965
94 Yang H, Zhang Y, Pan J, *et al.* Room-temperature engineering of all-inorganic perovskite nanocrsytals with different dimensionalities. Chem Mater, 2017, 29: 8978–8982
95 Wen JR, Roman BJ, Rodriguez Ortiz FA, *et al.* Chemical availability of bromide dictates $CsPbBr_3$ nanocrystal growth. Chem Mater, 2019, 31: 8551–8557
96 Akkerman QA, Abdelhady AL, Manna L. Zero-dimensional cesium lead halides: History, properties, and challenges. J Phys Chem Lett, 2018, 9: 2326–2337
97 Shyamal S, Dutta SK, Das T, *et al.* Facets and defects in perovskite nanocrystals for photocatalytic CO_2 reduction. J Phys Chem Lett, 2020, 11: 3608–3614
98 Bera S, Behera RK, Pradhan N. α-Halo ketone for polyhedral perovskite nanocrystals: Evolutions, shape conversions, ligand chemistry, and self-assembly. J Am Chem Soc, 2020, 142: 20865–20874
99 Baranov D, Lynch MJ, Curtis AC, *et al.* Purification of oleylamine for materials synthesis and spectroscopic diagnostics for *trans* isomers. Chem Mater, 2019, 31: 1223–1230
100 Yassitepe E, Yang Z, Voznyy O, *et al.* Amine-free synthesis of cesium lead halide perovskite quantum dots for efficient light-emitting diodes. Adv Funct Mater, 2016, 26: 8757–8763
101 Tan Y, Zou Y, Wu L, *et al.* Highly luminescent and stable perovskite nanocrystals with octylphosphonic acid as a ligand for efficient light-emitting diodes. ACS Appl Mater Interfaces, 2018, 10: 3784–3792
102 Seth S, Samanta A. A facile methodology for engineering the morphology of $CsPbX_3$ perovskite nanocrystals under ambient condition. Sci Rep, 2016, 6: 37693
103 de la Hoz A, Díaz-Ortiz Á, Moreno A. Microwaves in organic synthesis. Thermal and non-thermal microwave effects. Chem Soc Rev, 2005, 34: 164–178
104 Zhu YJ, Chen F. Microwave-assisted preparation of inorganic nanostructures in liquid phase. Chem Rev, 2014, 114: 6462–6555
105 Rao L, Ding X, Du X, *et al.* Ultrasonication-assisted synthesis of $CsPbBr_3$ and Cs_4PbBr_6 perovskite nanocrystals and their reversible transformation. Beilstein J Nanotechnol, 2019, 10: 666–676
106 Li Y, Huang H, Xiong Y, *et al.* Using polar alcohols for the direct synthesis of cesium lead halide perovskite nanorods with anisotropic emission. ACS Nano, 2019, 13: 8237–8245
107 Ng CK, Yin W, Li H, *et al.* Scalable synthesis of colloidal $CsPbBr_3$ perovskite nanocrystals with high reaction yields through solvent and ligand engineering. Nanoscale, 2020, 12: 4859–4867
108 Li Z, Najeeb MA, Alves L, *et al.* Robot-accelerated perovskite in-

vestigation and discovery. Chem Mater, 2020, 32: 5650–5663

109 Gu E, Tang X, Langner S, *et al.* Robot-based high-throughput screening of antisolvents for lead halide perovskites. Joule, 2020, 4: 1806–1822

110 Kang J, Wang LW. High defect tolerance in lead halide perovskite $CsPbBr_3$. J Phys Chem Lett, 2017, 8: 489–493

111 Swarnkar A, Chulliyil R, Ravi VK, *et al.* Colloidal $CsPbBr_3$ perovskite nanocrystals: Luminescence beyond traditional quantum dots. Angew Chem Int Ed, 2015, 54: 15424–15428

112 Akkerman QA, D'Innocenzo V, Accornero S, *et al.* Tuning the optical properties of cesium lead halide perovskite nanocrystals by anion exchange reactions. J Am Chem Soc, 2015, 137: 10276–10281

113 Mondal N, De A, Samanta A. Achieving near-unity photoluminescence efficiency for blue-violet-emitting perovskite nanocrystals. ACS Energy Lett, 2019, 4: 32–39

114 Huang G, Wang C, Xu S, *et al.* Postsynthetic doping of $MnCl_2$ molecules into preformed $CsPbBr_3$ perovskite nanocrystals *via* a halide exchange-driven cation exchange. Adv Mater, 2017, 29: 1700095

115 Liu H, Wu Z, Shao J, *et al.* $CsPb_xMn_{1-x}Cl_3$ perovskite quantum dots with high Mn substitution ratio. ACS Nano, 2017, 11: 2239–2247

116 Mir WJ, Mahor Y, Lohar A, *et al.* Postsynthesis doping of Mn and Yb into $CsPbX_3$ (X = Cl, Br, or I) perovskite nanocrystals for downconversion emission. Chem Mater, 2018, 30: 8170–8178

117 Begum R, Parida MR, Abdelhady AL, *et al.* Engineering interfacial charge transfer in $CsPbBr_3$ perovskite nanocrystals by heterovalent doping. J Am Chem Soc, 2017, 139: 731–737

118 Liu M, Zhong G, Yin Y, *et al.* Aluminum-doped cesium lead bromide perovskite nanocrystals with stable blue photoluminescence used for display backlight. Adv Sci, 2017, 4: 1700335

119 Ling Y, Tan L, Wang X, *et al.* Composite perovskites of cesium lead bromide for optimized photoluminescence. J Phys Chem Lett, 2017, 8: 3266–3271

120 Scheidt RA, Kerns E, Kamat PV. Interfacial charge transfer between excited $CsPbBr_3$ nanocrystals and TiO_2: Charge injection *versus* photodegradation. J Phys Chem Lett, 2018, 9: 5962–5969

121 Lu C, Li H, Kolodziejski K, *et al.* Enhanced stabilization of inorganic cesium lead triiodide ($CsPbI_3$) perovskite quantum dots with tri-octylphosphine. Nano Res, 2018, 11: 762–768

122 Song L, Guo X, Hu Y, *et al.* Efficient inorganic perovskite light-emitting diodes with polyethylene glycol passivated ultrathin $CsPbBr_3$ films. J Phys Chem Lett, 2017, 8: 4148–4154

123 Wang Y, Zhang T, Kan M, *et al.* Bifunctional stabilization of all-inorganic α-$CsPbI_3$ perovskite for 17% efficiency photovoltaics. J Am Chem Soc, 2018, 140: 12345–12348

124 Zhang Q, Zhou Y, Wei Y, *et al.* Improved phase stability of γ-$CsPbI_3$ perovskite nanocrystals using the interface effect using iodine modified graphene oxide. J Mater Chem C, 2020, 8: 2569–2578

125 Wang H, Fang J, Cheng T, *et al.* One-step coating of fluoro-containing silicananoparticles for universal generation of surface superhydrophobicity. Chem Commun, 2008, 877–879

126 Zhang F, Shi ZF, Ma ZZ, *et al.* Silica coating enhances the stability of inorganic perovskite nanocrystals for efficient and stable down-conversion in white light-emitting devices. Nanoscale, 2018, 10: 20131–20139

127 Loiudice A, Saris S, Oveisi E, *et al.* $CsPbBr_3$ QD/AlO_x inorganic nanocomposites with exceptional stability in water, light, and heat. Angew Chem Int Ed, 2017, 56: 10696–10701

128 Zhang F, Shi Z, Li S, *et al.* Synergetic effect of the surfactant and silica coating on the enhanced emission and stability of perovskite quantum dots for anticounterfeiting. ACS Appl Mater Interfaces, 2019, 11: 28013–28022

129 Park DH, Han JS, Kim W, *et al.* Facile synthesis of thermally stable $CsPbBr_3$ perovskite quantum dot-inorganic SiO_2 composites and their application to white light-emitting diodes with wide color gamut. Dyes Pigments, 2018, 149: 246–252

130 Zheng Z, Liu L, Yi F, *et al.* Significantly improving the moisture-, oxygen- and thermal-induced photoluminescence in all-inorganic halide perovskite $CsPbI_3$ crystals by coating the SiO_2 layer. J Lumin, 2019, 216: 116722

131 Li ZJ, Hofman E, Li J, *et al.* Photoelectrochemically active and environmentally stable $CsPbBr_3$/TiO_2 core/shell nanocrystals. Adv Funct Mater, 2018, 28: 1704288

132 Xu Y, Wang X, Liao J, *et al.* Amorphous-TiO_2-encapsulated $CsPbBr_3$ nanocrystal composite photocatalyst with enhanced charge separation and CO_2 fixation. Adv Mater Interfaces, 2018, 5: 1801015

133 Liao JF, Xu YF, Wang XD, *et al.* $CsPbBr_3$ nanocrystal/MO_2 (M = Si, Ti, Sn) composites: Insight into charge-carrier dynamics and photoelectrochemical applications. ACS Appl Mater Interfaces, 2018, 10: 42301–42309

134 Zhong Q, Cao M, Hu H, *et al.* One-pot synthesis of highly stable $CsPbBr_3$@SiO_2 core-shell nanoparticles. ACS Nano, 2018, 12: 8579–8587

135 Stranks SD, Eperon GE, Grancini G, *et al.* Electron-hole diffusion lengths exceeding 1 micrometer in an organometal trihalide perovskite absorber. Science, 2013, 342: 341–344

136 Fang Y, Dong Q, Shao Y, *et al.* Highly narrowband perovskite single-crystal photodetectors enabled by surface-charge recombination. Nat Photon, 2015, 9: 679–686

137 Knezevic M, Quach DV, Lampre I, *et al.* Adjusting the band gap of $CsPbBr_{3-y}X_y$ (X = Cl, I) for optimal interfacial charge transfer and enhanced photocatalytic hydrogen generation. J Mater Chem, 2023, 11: 6226–6236

138 Diroll BT, Nedelcu G, Kovalenko MV, *et al.* High-temperature photoluminescence of $CsPbX_3$ (X = Cl, Br, I) nanocrystals. Adv Funct Mater, 2017, 27: 1606750

139 Yettapu GR, Talukdar D, Sarkar S, *et al.* Terahertz conductivity within colloidal $CsPbBr_3$ perovskite nanocrystals: Remarkably high carrier mobilities and large diffusion lengths. Nano Lett, 2016, 16: 4838–4848

140 Sarkar S, Ravi VK, Banerjee S, *et al.* Terahertz spectroscopic probe of hot electron and hole transfer from colloidal $CsPbBr_3$ perovskite nanocrystals. Nano Lett, 2017, 17: 5402–5407

141 Zhai Y, Wang K, Zhang F, *et al.* Individual electron and hole mobilities in lead-halide perovskites revealed by noncontact methods. ACS Energy Lett, 2020, 5: 47–55

142 Hutter EM, Savenije TJ. Thermally activated second-order recombination hints toward indirect recombination in fully inorganic $CsPbI_3$ perovskites. ACS Energy Lett, 2018, 3: 2068–2069

143 Gaulding EA, Hao J, Kang HS, *et al.* Conductivity tuning *via* doping with electron donating and withdrawing molecules in perovskite $CsPbI_3$ nanocrystal films. Adv Mater, 2019, 31: 1902250

144 Boehme SC, Brinck S, Maes J, *et al.* Phonon-mediated and weakly size-dependent electron and hole cooling in $CsPbBr_3$ nanocrystals revealed by atomistic simulations and ultrafast spectroscopy. Nano Lett, 2020, 20: 1819–1829

145 Kobiyama E, Tahara H, Sato R, *et al.* Reduction of optical gain threshold in $CsPbI_3$ nanocrystals achieved by generation of asymmetric hot-biexcitons. Nano Lett, 2020, 20: 3905–3910

146 Hopper T, Gorodetsky A, Krieg F, *et al.* Hot-carrier cooling in lead-bromide perovskite materials. In: Proceedings of the Physical Chemistry of Semiconductor Materials and Interfaces XVIII. San Diego, California: SPIE, 2019. 13

147 Li Y, Luo X, Liu Y, *et al.* Size- and composition-dependent exciton spin relaxation in lead halide perovskite quantum dots. ACS Energy Lett, 2020, 5: 1701–1708

148 Butkus J, Vashishtha P, Chen K, *et al.* The evolution of quantum confinement in $CsPbBr_3$ perovskite nanocrystals. Chem Mater, 2017, 29: 3644–3652

149 Chung H, Jung SI, Kim HJ, *et al.* Composition-dependent hot carrier relaxation dynamics in cesium lead halide ($CsPbX_3$, X = Br and I) perovskite nanocrystals. Angew Chem Int Ed, 2017, 56: 4160–4164

150 Chen J, Messing ME, Zheng K, *et al.* Cation-dependent hot carrier cooling in halide perovskite nanocrystals. J Am Chem Soc, 2019, 141: 3532–3540

151 Mondal A, Aneesh J, Kumar Ravi V, *et al.* Ultrafast exciton many-body interactions and hot-phonon bottleneck in colloidal cesium lead halide perovskite nanocrystals. Phys Rev B, 2018, 98: 115418

152 Mondal N, Samanta A. Complete ultrafast charge carrier dynamics in photo-excited all-inorganic perovskite nanocrystals ($CsPbX_3$). Na-

noscale, 2017, 9: 1878–1885

153 Castañeda JA, Nagamine G, Yassitepe E, *et al.* Efficient biexciton interaction in perovskite quantum dots under weak and strong confinement. ACS Nano, 2016, 10: 8603–8609

154 Kaur G, Ghosh HN. Hot carrier relaxation in CsPbBr$_3$-based perovskites: A polaron perspective. J Phys Chem Lett, 2020, 11: 8765–8776

155 Rossi D, Wang H, Dong Y, *et al.* Light-induced activation of forbidden exciton transition in strongly confined perovskite quantum dots. ACS Nano, 2018, 12: 12436–12443

156 Li Y, Lai R, Luo X, *et al.* On the absence of a phonon bottleneck in strongly confined CsPbBr$_3$ perovskite nanocrystals. Chem Sci, 2019, 10: 5983–5989

157 Madjet ME, Berdiyorov GR, El-Mellouhi F, *et al.* Cation effect on hot carrier cooling in halide perovskite materials. J Phys Chem Lett, 2017, 8: 4439–4445

158 Soetan N, Puretzky A, Reid K, *et al.* Ultrafast spectral dynamics of CsPb(Br$_x$Cl$_{1-x}$)$_3$ mixed-halide nanocrystals. ACS Photonics, 2018, 5: 3575–3583

159 Mandal S, Ghosh S, Mukherjee S, *et al.* Unravelling halide-dependent charge carrier dynamics in CsPb(Br/Cl)$_3$ perovskite nanocrystals. Nanoscale, 2021, 13: 3654–3661

160 Wang S, Leng J, Yin Y, *et al.* Ultrafast dopant-induced exciton auger-like recombination in Mn-doped perovskite nanocrystals. ACS Energy Lett, 2020, 5: 328–334

161 Justice Babu K, Kaur G, Shukla A, *et al.* Concurrent energy- and electron-transfer dynamics in photoexcited Mn-doped CsPbBr$_3$ perovskite nanoplatelet architecture. J Phys Chem Lett, 2021, 12: 302–309

162 Ketavath R, Katturi NK, Ghugal SG, *et al.* Deciphering the ultrafast nonlinear optical properties and dynamics of pristine and Ni-doped CsPbBr$_3$ colloidal two-dimensional nanocrystals. J Phys Chem Lett, 2019, 10: 5577–5584

163 Nenon DP, Pressler K, Kang J, *et al.* Design principles for trap-free CsPbX$_3$ nanocrystals: Enumerating and eliminating surface halide vacancies with softer lewis bases. J Am Chem Soc, 2018, 140: 17760–17772

164 Nan G, Zhang X, Abdi-Jalebi M, *et al.* How methylammonium cations and chlorine dopants heal defects in lead iodide perovskites. Adv Energy Mater, 2018, 8: 1702754

165 Guo JJ, Zhao HY, Ai LY, *et al.* B$_{12}$@Mg$_{20}$Al$_{12}$ core-shell molecule: A candidate for high-capacity hydrogen storage material. Int J Hydrogen Energy, 2019, 44: 28235–28241

166 Brzhezinskaya M, Svechnikov NY, Stankevich VG, *et al.* Characterization of amorphous hydrocarbon CD$_x$ films ($x \sim 0.5$) for energy storage applications. Fullerenes Nanotubes Carbon NanoStruct, 2020, 28: 173–178

167 Al S. Investigations of physical properties of XTiH$_3$ and implications for solid state hydrogen storage. Z für Naturforschung A, 2019, 74: 1023–1030

168 Li J, Wang L, Yuan X, *et al.* Ultraviolet light induced degradation of luminescence in CsPbBr$_3$ perovskite nanocrystals. Mater Res Bull, 2018, 102: 86–91

169 Ye Q, Zhao Y, Mu S, *et al.* Stabilizing the black phase of cesium lead halide inorganic perovskite for efficient solar cells. Sci China Chem, 2019, 62: 810–821

170 Dutta A, Pradhan N. Phase-stable red-emitting CsPbI$_3$ nanocrystals: Successes and challenges. ACS Energy Lett, 2019, 4: 709–719

171 Yang MZ, Xu YF, Liao JF, *et al.* Constructing CsPbBr$_x$I$_{3-x}$ nanocrystal/carbon nanotube composites with improved charge transfer and light harvesting for enhanced photoelectrochemical activity. J Mater Chem A, 2019, 7: 5409–5415

172 Kong ZC, Liao JF, Dong YJ, *et al.* Core@shell CsPbBr$_3$@zeolitic imidazolate framework nanocomposite for efficient photocatalytic CO$_2$ reduction. ACS Energy Lett, 2018, 3: 2656–2662

173 Kong ZC, Zhang HH, Liao JF, *et al.* Immobilizing Re(CO)$_3$Br(dcbpy) complex on CsPbBr$_3$ nanocrystal for boosted charge separation and photocatalytic CO$_2$ reduction. Sol RRL, 2020, 4: 1900365

174 Song W, Wang Y, Wang C, *et al.* Photocatalytic hydrogen production by stable CsPbBr$_3$@PANI nanoparticles in aqueous solution. ChemCatChem, 2021, 13: 1711–1716

175 Corti M, Bonomi S, Chiara R, *et al.* Application of metal halide perovskites as photocatalysts in organic reactions. Inorganics, 2021, 9: 56

176 Xu Y, Zhang W, Su K, *et al.* Glycine-functionalized CsPbBr$_3$ nanocrystals for efficient visible-light photocatalysis of CO$_2$ reduction. Chem Eur J, 2021, 27: 2305–2309

177 Li Y, Shu Q, Du Q, *et al.* Surface modification for improving the photocatalytic polymerization of 3,4-ethylenedioxythiophene over inorganic lead halide perovskite quantum dots. ACS Appl Mater Interfaces, 2020, 12: 451–460

178 Wu LY, Zhang MR, Feng YX, *et al.* Two-dimensional metal halide perovskite nanosheets for efficient photocatalytic CO$_2$ reduction. Sol RRL, 2021, 5: 2100263

179 Guo SH, Zhou J, Zhao X, *et al.* Enhanced CO$_2$ photoreduction *via* tuning halides in perovskites. J Catal, 2019, 369: 201–208

180 Shyamal S, Dutta SK, Pradhan N. Doping iron in CsPbBr$_3$ perovskite nanocrystals for efficient and product selective CO$_2$ reduction. J Phys Chem Lett, 2019, 10: 7965–7969

181 Liu YW, Guo SH, You SQ, *et al.* Mn-doped CsPb(Br/Cl)$_3$ mixed-halide perovskites for CO$_2$ photoreduction. Nanotechnology, 2020, 31: 215605

182 Mu Y, Zhang W, Guo X, *et al.* Water-tolerant lead halide perovskite nanocrystals as efficient photocatalysts for visible-light-driven CO$_2$ reduction in pure water. ChemSusChem, 2019, 12: 4769–4774

183 Ding L, Shen C, Zhao Y, *et al.* CsPbBr$_3$ nanocrystals glass facilitated with Zn ions for photocatalytic hydrogen production *via* H$_2$O splitting. Mol Catal, 2020, 483: 110764

184 Chen Z, Hu Y, Wang J, *et al.* Boosting photocatalytic CO$_2$ reduction on CsPbBr$_3$ perovskite nanocrystals by immobilizing metal complexes. Chem Mater, 2020, 32: 1517–1525

185 Xu YF, Yang MZ, Chen BX, *et al.* A CsPbBr$_3$ perovskite quantum dot/graphene oxide composite for photocatalytic CO$_2$ reduction. J Am Chem Soc, 2017, 139: 5660–5663

186 Xu YF, Yang MZ, Chen HY, *et al.* Enhanced solar-driven gaseous CO$_2$ conversion by CsPbBr$_3$ nanocrystal/pd nanosheet Schottky-junction photocatalyst. ACS Appl Energy Mater, 2018, 1: 5083–5089

187 Kobosko SM, DuBose JT, Kamat PV. Perovskite photocatalysis. Methyl viologen induces unusually long-lived charge carrier separation in CsPbBr$_3$ nanocrystals. ACS Energy Lett, 2020, 5: 221–223

188 DuBose JT, Kamat PV. Probing perovskite photocatalysis. Interfacial electron transfer between CsPbBr$_3$ and ferrocene redox couple. J Phys Chem Lett, 2019, 10: 6074–6080

189 Li L, Zhang Z, Ding C, *et al.* Boosting charge separation and photocatalytic CO$_2$ reduction of CsPbBr$_3$ perovskite quantum dots by hybridizing with P3HT. Chem Eng J, 2021, 419: 129543

190 Zhang Z, Shu M, Jiang Y, *et al.* Fullerene modified CsPbBr$_3$ perovskite nanocrystals for efficient charge separation and photocatalytic CO$_2$ reduction. Chem Eng J, 2021, 414: 128889

191 Pan A, Ma X, Huang S, *et al.* CsPbBr$_3$ perovskite nanocrystal grown on MXene nanosheets for enhanced photoelectric detection and photocatalytic CO$_2$ reduction. J Phys Chem Lett, 2019, 10: 6590–6597

192 Ou M, Tu W, Yin S, *et al.* Amino-assisted anchoring of CsPbBr$_3$ perovskite quantum dots on porous g-C$_3$N$_4$ for enhanced photocatalytic CO$_2$ reduction. Angew Chem Int Ed, 2018, 57: 13570–13574

193 Zhou L. Fundamentals of combustion theory. Theory Model Dispersed Multiph Turbul React Flows, 2018: 15–70, doi: 10.1016/B978-0-12-813465-8.00003-X

194 Guo XX, Tang SF, Mu YF, *et al.* Engineering a CsPbBr$_3$-based nanocomposite for efficient photocatalytic CO$_2$ reduction: Improved charge separation concomitant with increased activity sites. RSC Adv, 2019, 9: 34342–34348

195 Su K, Dong GX, Zhang W, *et al.* *In situ* coating CsPbBr$_3$ nanocrystals with graphdiyne to boost the activity and stability of photocatalytic CO$_2$ reduction. ACS Appl Mater Interfaces, 2020, 12: 50464–50471

196 Gu K, Wang Y, Shen J, *et al.* Effective singlet oxygen generation in silica-coated CsPbBr$_3$ quantum dots through energy transfer for photocatalysis. ChemSusChem, 2020, 13: 682–687

197 Sun Q, Xu J, Tao F, *et al.* Boosted inner surface charge transfer in perovskite nanodots@mesoporous titania frameworks for efficient and

selective photocatalytic CO_2 reduction to methane. Angew Chem Int Ed, 2022, 61: e202200872
198 Mu Y, Zhang W, Dong G, *et al.* Ultrathin and small-size graphene oxide as an electron mediator for perovskite-based Z-scheme system to significantly enhance photocatalytic CO_2 reduction. Small, 2020, 16: 2002140
199 Tang R, Zhou S, Li H, *et al.* Halogen bonding induced aqueously stable $CsPbBr_3$@MOFs-derived Co_3O_4/N-doped-C heterostructure for high-performance photoelectrochemical water oxidation. Appl Catal B-Environ, 2020, 265: 118583
200 Chen ZY, Hong QL, Zhang HX, *et al.* Composite of $CsPbBr_3$ with boron imidazolate frameworks as an efficient visible-light photocatalyst for CO_2 reduction. ACS Appl Energy Mater, 2022, 5: 1175–1182

Acknowledgements Knezevic M acknowledges the «Ministère de l'enseignement supérieur et de la recherche Français» for the PhD grant. Knezevic M, Colbeau-Justin C, and Ghazzal MN acknowledge the IDEX Paris-Saclay and IRS MOMENTOM for financial support. Ghazzal MN thanks the French National Research Agency (ANR), through the IngenCat project (ANR-20-CE43-0014), for the financial support. The authors acknowledge the ACT programme (Accelerating CCS Technologies, Horizon2020 Project No. 691712) for the financial support of the NEXTCCUS project (project ID: 327327). Abdi-Jalebi M acknowledges the Royal Society (RGS\R1\211068) and Cambridge Materials Limited for their funding and technical support. Abdi-Jalebi M and Rashid N acknowledge the Department for Energy Security and Net Zero (Project ID: NEXTCCUS), University College London's Research, Innovation and Global Engagement, and UCL Cities Partnerships Programme Award in Paris for their financial support.

Author contributions Knezevic M wrote the first draft. Hoang TH contributed to writing the first draft. Rashid N and Abdi-Jalebi M helped review the manuscript and commented on the review. Colbeau-Justin C and Ghazzal MN supervised the work. Ghazzal MN and Knezevic M reviewed the manuscript and finalized the final version. The manuscript was written through the contributions of all authors.

Conflict of interest The authors declare that they have no conflict of interest.

Marija Knezevic is a PhD student in materials science at Institut de Chimie Physique, Université Paris-Saclay. Her research focuses on metal-halide perovskites' charge-carrier dynamics and their application in photocatalysis.

Thi-Hieu Hoang obtained her Bachelor's degree from Hanoi University of Science, Vietnam in 2021. Then, she received the IDEX scholarship for two years of master program and became a student at Université Paris-Saclay.

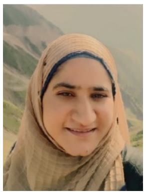

Nusrat Rashid obtained her PhD degree in chemistry at Indian Institute of Technology Delhi, India. Her research focuses on the development of industrially viable electrochemical systems for direct CO_2 conversion to methanol. Currently, she is formulating earth-abundant n-type semiconductors as prospectus anode cores for sustainable, direct and cost-effective photovoltaic-electrochemical (PV-EC) CO_2 electrolyzers for net negative greenhouse gas emissions in accordance with the circular carbon economy.

Mojtaba Abdi-Jalebi is an assistant professor in energy materials at the Institute for Materials Discovery, the Faculty of Mathematical and Physical Sciences, the University College London (UCL). Since November 2019, his research has focused on material and electronic properties of emerging semiconductors including halide perovskites, small molecules, and organic semiconductors for low-cost optoelectronic and electrochemical devices for low-cost electronics applications and energy systems enabling carbon capture and production of solar fuels.

Christophe Colbeau-Justin is currently a full professor at the Institut de Chimie Physique, Université Paris-Saclay, Orsay, France, where he is studying charge-carrier dynamics in photoactive materials.

Mohamed Nawfal Ghazzal is an associate professor at the Université Paris-Saclay. He is now investigating strategies aiming at realizing the utilization of perovskites for photocatalytic application, synthesizing new carbon-based materials and developing new bio-inspired architectures for improved charge carriers' lifetime and light harvesting capability. The main goal is to establish a relationship between material chemistry and design, dynamics of photogenerated charge carriers, and chemical reactions in photocatalytic processes.